

SAND REPORT

SAND2002-8285
Unlimited Release
Printed June 2002

High-Rate Shear Deformation and Failure in Structural Alloys

D. B. Dawson, R. A. Regueiro, Y. Ohashi, G. Ravichandran, M. Viral

Prepared by
Sandia National Laboratories
Albuquerque, New Mexico 87185 and Livermore, California 94550

Sandia is a multiprogram laboratory operated by Sandia Corporation,
a Lockheed Martin Company, for the United States Department of
Energy under Contract DE-AC04-94AL85000.

Approved for public release; further dissemination unlimited.



Sandia National Laboratories

Issued by Sandia National Laboratories, operated for the United States Department of Energy by Sandia Corporation.

NOTICE: This report was prepared as an account of work sponsored by an agency of the United States Government. Neither the United States Government, nor any agency thereof, nor any of their employees, nor any of their contractors, subcontractors, or their employees, make any warranty, express or implied, or assume any legal liability or responsibility for the accuracy, completeness, or usefulness of any information, apparatus, product, or process disclosed, or represent that its use would not infringe privately owned rights. Reference herein to any specific commercial product, process, or service by trade name, trademark, manufacturer, or otherwise, does not necessarily constitute or imply its endorsement, recommendation, or favoring by the United States Government, any agency thereof, or any of their contractors or subcontractors. The views and opinions expressed herein do not necessarily state or reflect those of the United States Government, any agency thereof, or any of their contractors.

Printed in the United States of America. This report has been reproduced directly from the best available copy.

Available to DOE and DOE contractors from

U.S. Department of Energy
Office of Scientific and Technical Information
P.O. Box 62
Oak Ridge, TN 37831

Telephone: (865)576-8401
Facsimile: (865)576-5728
E-Mail: reports@adonis.osti.gov
Online ordering: <http://www.doe.gov/bridge>

Available to the public from

U.S. Department of Commerce
National Technical Information Service
5285 Port Royal Rd
Springfield, VA 22161

Telephone: (800)553-6847
Facsimile: (703)605-6900
E-Mail: orders@ntis.fedworld.gov
Online order: <http://www.ntis.gov/ordering.htm>



SAND2002-8285
Unlimited Release
Printed June 2002

High-Rate Shear Deformation and Failure in Structural Alloys

Daniel B. Dawson
Materials Mechanics Department

Richard A. Regueiro
Science-Based Materials Modeling Department

Yuki Ohashi
Engineering Mechanics Modeling and Simulation Department

Sandia National Laboratories
Livermore, CA 94551-0969

G. Ravichandran and Murat Viral
California Institute of Technology
Graduate Aeronautical Laboratories
Pasadena, CA

Abstract

Experiments were conducted to determine the dynamic shear behavior of a wide range of aluminum, titanium, and steel alloys. Principal experimental techniques were the torsional Kolsky bar and the Shear Compression Specimen (SCS) geometry. For the purpose of determining adiabatic shear susceptibility in this range of alloys, it was found that both techniques were unable to induce adiabatic shear in alloys resistant to that failure mode. The SCS geometry has demonstrated a capability for characterizing shear deformation behavior over a wide range of strain rates. For modeling and simulation of adiabatic shear phenomena, an improved adiabatic temperature evolution equation has been implemented. Finite element simulations of the torsional Kolsky and SCS geometries were conducted to evaluate the influence of pre-existing geometric inhomogeneities on adiabatic shear band initiation.

Acknowledgements

At the California Institute of Technology, major contributions to the development of the shear-compression specimen and its application to adiabatic shear testing were made by Dr. S. Lee (now at Motorola Corp.), and by Dr. D. Rittel while on a sabbatical leave from Technion, Israel Institute of Technology. At Sandia, Jay Dike (Engineering Mechanics Modeling and Simulation Department) was responsible for computational simulations in the early stages of this project. Andy Gardea (Analytical Materials Science Department) demonstrated ingenuity in the difficult task of providing metallographic evidence of adiabatic shear banding in test specimens.

Contents

Introduction.....	7
Background.....	7
Adiabatic Shear Occurrence	7
Adiabatic Shear Band Characteristics	10
Experimental Background	11
Modeling Background	12
Experimental Procedure and Results	14
Materials	14
Specimen Evaluation	15
Double Linear Shear	16
Torsional Kolsky Technique.....	17
Shear Compression Specimen	20
SCS Experimental Results: Shear Deformation and Failure	24
Modeling and Simulation	35
Adiabatic Temperature Evolution.....	36
Simulation of Torsional Kolsky and SCS Specimens	36
Coupled Elastodynamic/Heat Conduction Analysis.....	46
Discussion.....	48
Conclusions and Recommendations	49
References.....	50
Distribution	

List of Tables

1. Chemical Composition of Alloys	14
2. Mechanical Properties of Alloys	15
3. Other Material Constants for Ti-6Al-4V	39

List of Figures

1. Eroded nose of 4340 projectile.	8
2. Segmented Be-Cu chip formed in explosive valve.....	9
3. Double Linear Shear specimen.....	16
4. TSHB specimen with straight shoulders.....	17
5. Torsional Kolsky specimen with 45° shoulders.	18
6. Cross-section of 2024-T3 torsional Kolsky specimen.....	19
7. Original design for Shear Compression Specimen with $H/D = 3$	20
8. Modified SCS design with $H/D = 1.6$	21
9. SCS specimens showing lateral displacement.....	22
10. Variation in slot width for SCS specimens.....	23
11. Effect of strain rate on flow stress for 1018 steel: SCS specimens.	24
12. Effect of strain rate on flow stress for 1018 steel: cylindrical specimens.	25

List of Figures (continued)

13. Effect of strain rate on flow stress for 1018 steel: SCS vs. cylindrical.	25
14. Effect of strain rate on flow stress for A36 hot rolled steel.....	26
15. Effect of strain rate on flow stress for 18Ni300 Maraging steel.....	27
16. Effect of strain rate on flow stress for CP Titanium – Grade 2.	27
17. Effect of strain rate on flow stress for Ti6Al-4V.....	28
18. Effect of strain rate on flow stress for 6061-T6.....	28
19. Effect of strain rate on flow stress for 2024-T3.....	29
20. Effect of strain rate on flow stress for 7075-T6.....	30
21. Non-adiabatic shear localization in 6061-T6.....	31
22. Adiabatic shear bands near fracture surface for 18Ni300 Maraging steel.....	32
23. Cross-section of 1018 steel specimen that failed at 8000/s.	33
24. Cross-section of 1018 steel specimen that didn't fail at 4000/s.	34
25. Simulation of 6061-T6 SCS Experiment.....	37
26. Contour plots for 6061-T6 SCS specimen simulation.....	38
27. Comparison of Ti-6Al-4V experimental data and BCJ model	38
28. Full 3D simulation of Ti-6Al-4V torsional Kolsky specimen.	40
29. Slice simulation approximation of Ti-6Al-4V torsional Kolsky specimen.	41
30. Comparison of Pronto3D and Abaqus Explicit uniaxial compression.	42
31. Pronto 3D slice simulations: mesh refinement effects.	43
32. Abaqus Explicit slice simulation contour plots.	44
33. Force vs. displacement and shear stress/strain: Pronto 3D vs. Abaqus Explicit	45
34. Abaqus Explicit contour plots: coupled elastodynamic/heat conduction	46
35. Uncoupled and coupled Abaqus Explicit slice simulations.....	47

Introduction

Adiabatic shear is an extreme and usually catastrophic low-energy form of localized deformation that often occurs with dynamic loading conditions. In structural alloys of the types used in Sandia weapons applications, adiabatic shear failures are most commonly observed in blast and impact phenomena, ballistic penetration, and high-rate deformation processing and machining. Existing data (e.g. Timothy 1987) show that most structural alloys of interest for Sandia applications are susceptible to some degree. There are differences in adiabatic shear susceptibility, however: more resistant alloys (304 stainless steel, 5083 aluminum) require higher strains and/or higher strain rates to initiate adiabatic shear than less resistant ones (2024 aluminum, 4340 steel, Ti-6Al-4V). Some aspects of the adiabatic shear process and factors promoting susceptibility are known, but clearly defined susceptibility criteria for specific alloys and accurate phenomenological and computational models do not exist.

This report documents efforts to utilize existing dynamic shear test methods and/or develop new methods for the purpose of providing quantitative measures of critical conditions at the inception point of shear band formation. To support this experimental effort, modeling and simulation of adiabatic shear failure was performed for selected dynamic test techniques.

Background

As early as the 1940's, the effects that strain concentrations and localized increases in temperature could have on dynamic deformation were recognized, and the term "adiabatic shear band" was applied to the phenomenon (Zener & Hollomon 1944). For some period thereafter, adiabatic shear banding typically appeared in the literature only as an incidental observation associated with ballistic penetration, or occasionally high-speed metalworking. Greater interest started several decades ago, leading to experimental and analytical efforts that have expanded our knowledge of the diversity of its characteristics and its prevalence. However, predictive capability and accurate constitutive models of the phenomenon are still lacking. Published reviews that summarize adiabatic shear band phenomenology, test methods, and modeling issues include: Bedford et al. (1974), Rogers (1979), Rogers (1983), Stelly & Dormeval (1986), Timothy (1987), Bai & Dodd (1992).

Adiabatic Shear Occurrence

Early observations of adiabatic shear bands came from studies of ballistic impact and penetration, and metalworking processes. They are also seen in some types of frictional interfaces, such as impact abrasion. In ballistics, shear bands may be seen in both the

penetrator and the target (Backman & Goldsmith 1978; Meunier et al. 1992; Corbett et al. 1996). Figure 1 illustrates an example of adiabatic shear in the nose of a 4340 steel penetrator that impacted a concrete target (Hoke 1998). The SEM image in Fig. 1a shows the severely eroded nose. The cross-section micrograph in Fig. 1b shows narrow adiabatic shear bands at both the nose surface and sub-surface. They have the “white etching” appearance typical of such bands when they appear in high-strength steels.



Figure 1a: Eroded nose tip of 4340 steel projectile after penetration into concrete target. Material loss is both by surface erosion and sloughing-off of larger volumes of material. (Hoke 1998)



Figure 1b: Metallographic cross-section of eroded nose tip showing both adiabatic surface shear associated with erosion and subsurface adiabatic shear bands. Material subjected to adiabatic shear etches white in nital etch due to high-temperature phase transformation. (Hoke 1998)

In ballistic penetration of armor, penetrator nose shape (flat, ogive, hemispherical) has a strong influence on the type of failure and whether adiabatic shear bands will form in the target. A flat-nose configuration favors low-energy “plugging” penetration, a type of penetration failure that is frequently associated with shear banding (Wingrove 1973; Woodward 1984). Flat-nosed projectiles that are stepped to limit depth of penetration have been used to study the nature of adiabatic shear bands (Wingrove 1973; Grebe et al. 1985). Target alloys evaluated include steels (Rogers & Shastry 1981; Meunier et al. 1992; Dikshit et al. 1995), titanium alloys (Woodward et al. 1984; Grebe et al. 1985), and aluminum alloys (Wingrove 1973; Woodward et al. 1984; Leech 1985).

In metalworking processes, adiabatic shear bands are most commonly found in orthogonal metal cutting, high-rate forging, and punching/blanking/shearing operations. Recht (1964) studied adiabatic shear banding in high-speed machining of steel and titanium alloys and proposed an empirical failure criterion based on maximum shear stress. Segmented or discontinuous chip formation due to adiabatic shear was further studied for steels (Lemaier & Backofen 1972; Komanduri et al. 1982) and titanium alloys (Komanduri & Von Turkovich 1981; Bayoumi & Xie 1995). Figure 2 shows an example of segmented chip formation. In this case, it is formed in an explosive valve by the dynamic ploughing of a cylindrical high-strength steel plunger into the tapered bore of a Be-Cu valve housing. Ploughing of the flat-ended plunger forms an axisymmetric segmented Be-Cu chip similar to those produced in conventional orthogonal machining, with individual moderately-deformed segments separated by highly-deformed shear bands.

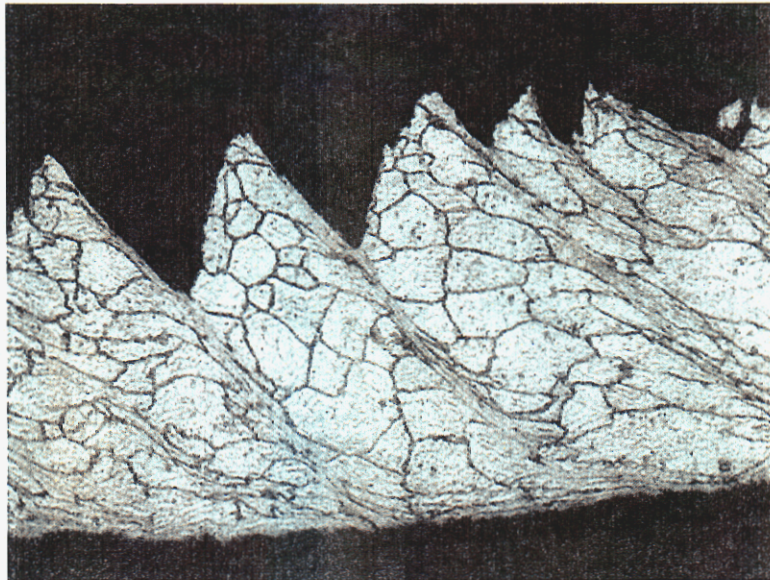


Figure 2: Segmented Be-Cu chip formed in explosive valve when cylindrical steel plunger ploughs into tapered bore in Be-Cu housing. Chip segments are separated by adiabatic shear bands

Some of the earliest observations of adiabatic shear were from the analysis of dynamic punching (Zener & Hollomon 1944), where it was shown that a major decrease in energy requirements for punching took place at high rates, where adiabatic shear occurred. Adiabatic shear banding in punching and shearing shows many similarities to adiabatic shear in the “plugging” failure mode that is seen in ballistic penetration (Bai & Johnson 1982). The geometry of the shear zone in punching facilitates the achievement of very high shearing rates. This has led to the use of punching geometries for a number of laboratory studies of adiabatic shearing, described below.

Adiabatic shear bands are observed in high-rate forging, particularly in upsetting operations (Semiati et al. 1983). For hot forging, processing maps have been developed for different alloys that identify temperature/strain-rate regimes to avoid, since adiabatic shear can occur (Prasad & Sasidhara 1997). Experiments to characterize high-rate forging behavior frequently make use of the Split-Hopkinson Pressure Bar technique. Adiabatic shear bands are also seen at interfaces involved in impact erosion or high-rate frictional contact (Bedford et al. 1974). Adiabatic “white etching” shear bands seen at the surface of the penetrator nose in Figure 1b are the result of erosion from frictional contact between the nose and the concrete target during penetration.

Adiabatic Shear Band Characteristics

“Adiabatic” here describes a situation where heat loss to areas outside an intense deformation zone is small compared to heat generation within the zone. In adiabatic shear, intense localization occurs when heat that is generated by an initial inhomogeneity in dynamic plastic strain causes a local rise in temperature. Thermal softening then overcomes the effects of strain hardening and strain rate hardening, an adiabatic shear band is triggered, and all subsequent dynamic deformation occurs in this high-temperature, rapidly-narrowing band as the thermal gradient and deformation gradient reinforce and sharpen each other. The critical importance of high rates and thermal-mechanical coupling of deformation and thermal softening distinguish this extreme form of deformation localization from other, less-catastrophic forms that occur under quasi-static isothermal conditions. Adiabatic shear also occurs most commonly for stress states that suppress localization associated with ductile void-nucleated fracture, a competing failure mode (Rogers 1979).

In an adiabatic shear band, local shear strains can be orders of magnitude greater than strains in areas adjacent to the band, while peak strain rates may be many orders magnitude higher. Local temperatures in the bands can be several hundred degrees or higher above adjacent areas. The bands are narrow, on the order of 10 to 100 μm in width. There are two types of adiabatic shear bands that have been classified as “deformation” type and “transformation” type (Backman & Finnegan 1973). Deformation-type bands are typical for aluminum alloys (Wingrove 1973; Leech 1985), austenitic steels, and low-strength ferritic steels. Transformation-type bands, which are typically much narrower than the deformation type, appear in alloys that undergo a high-temperature phase transformation, such as martensitic steels (Zener & Hollomon 1944; Rogers 1983) and titanium alloys (Wulf 1979). Alloys showing transformation bands

may also show deformation bands. In high-strength steels, untempered martensite in a transformation shear band appears white when the metallographic specimen is etched in nital (e.g., Figure 1b).

An important feature of adiabatic shear bands is that they are triggered by an initial localization of plastic deformation, after which thermal softening from the local temperature rise overcomes strain hardening and strain rate hardening, allowing the strain localization to sharpen and intensify. The significance of an initial localization as a triggering mechanism can be an advantage in designing certain types of adiabatic shear experiments (e.g., punch-type tests), but is a disadvantage in others since it leads to increased scatter and uncertainty in test results. The identification and characterization of material defects or stress concentrations that lead to initial localization is also an issue for modeling and simulation of adiabatic shear (Wright 1994; Batra, et al. 1996).

Experimental Background

A variety of experimental techniques have been used for evaluating dynamic effects on materials behavior, including adiabatic shear localization. Some of the experimental techniques used to date (e.g., ballistic penetration) are essentially phenomenological or qualitative in nature, while others yield quantitative information that can support the development of models or susceptibility criteria.

Dynamic compression tests are commonly used to characterize strain rate effects on materials, some of which exhibit adiabatic shear failures. Some early experiments were conducted using high-rate hydraulic compression apparatus that can achieve strain rates as high as 500/sec (Semiatin & Lahoti 1983). However, dynamic compression is more often conducted using the Split-Hopkinson Pressure Bar (SHPB), also called the compression Kolsky bar. SHPB studies related to adiabatic shear include Wulf (1979), Affouard et al. (1984), and Lee & Lin (1998).

To achieve higher strains and strain rates in axial impact under conditions closer to pure shear, the cylindrical compression specimen of earlier SHPB experiments was replaced with an axially-symmetric "top hat" specimen (Hartmann et al. 1981; Beatty et al. 1992). Loading of this adiabatic shear specimen could be with a compression Kolsky bar apparatus or a drop-weight impact machine. Punch experiments have also been conducted in the laboratory using Kolsky-type impact loading (Winter 1975, Zurek 1994; Mason et al. 1997; Roessig & Mason 1999). With suitable design of loading fixtures, a punch specimen that is much simpler than the top hat geometry can be used (Meyer & Manwaring 1986). A further development of the top hat was the flat "modified double shear" specimen, which is essentially a radial slice through the cylindrical top hat (Klepaczko 1994; Klepaczko 1998). Other types of double linear shear specimens include the flat doubly-notched bar used earlier by (Campbell & Ferguson 1970), and the modified doubly-notched Charpy specimen of Cowie et al. (1989). These adiabatic shear specimens are all designed to restrict plastic deformation to a very narrow gage section, where very high shear strains and strain rates can be achieved under impact loading.

Dynamic torsional loading can also be used to achieve high shear strains and strain rates. Early experiments included torsional impact loading (Culver 1972) and a high-speed hydraulic actuator (Lindholm et al. 1980). However, most high rate torsional loading is conducted using the torsional Kolsky bar technique (Gilat 2000). Initial applications were for evaluation of high strain-rate deformation behavior (Nicholas & Lawson 1972; Eleiche & Duffy 1975). More recently, this technique has been used for studying alloys that are susceptible to adiabatic shear (Marchand & Duffy 1988; Giovanola 1988a; Giovanola 1988b; Liao & Duffy 1998).

A specialized category of experiments looks at the dynamic extension of pre-existing cracks under impact loading (Kalthoff & Winkler 1988; Mason et al. 1994; Roessig & Mason 1998). In some cases, dynamic crack advance in these specimens involves adiabatic shearing. There are also techniques capable of achieving very high strain rates, i.e. 10^4 to 10^7 /sec, including explosive-driven contained expansion of cylinders (Staker 1981; Wittman et al. 1990), plate impact (Curran et al. 1987), and pressure-shear testing (Clifton & Klopp 1985).

Modeling Background

For the adiabatic shear process, first principles suggest the importance of factors and the external loading environment. Analytical models related to adiabatic thermophysical properties, mechanical properties and microstructure, and geometrical shear banding that incorporate some of these parameters have been developed. However, the relative importance of these factors and how they interplay in this dynamic process, with inherently tight coupling of temperature and mechanical fields, are poorly understood.

Zener & Hollomon (1944) recognized the essential process by which, at high rates of deformation, plastic shear instability occurs: localized thermal softening due to adiabatic (or near-adiabatic) heating overcomes strain hardening and strain-rate hardening. With certain simplifying assumptions, the increment in shear stress can be written as (Bai & Dodd 1992):

$$d\tau = \left(\frac{\partial \tau}{\partial \gamma} \right)_{\dot{\gamma}, \theta} d\gamma + \left(\frac{\partial \tau}{\partial \dot{\gamma}} \right)_{\gamma, \theta} d\dot{\gamma} + \left(\frac{\partial \tau}{\partial \theta} \right)_{\gamma, \dot{\gamma}} d\theta \quad (1)$$

where τ is shear stress, γ and $\dot{\gamma}$ are shear strain and shear strain rate, and θ is temperature. The three differential terms represent strain hardening, strain-rate hardening, and thermal softening, respectively. Assuming that adiabatic shear initiates at $d\tau = 0$ (maximum stress) and that strain-rate hardening effects can be neglected in comparison to the effects of strain hardening and thermal softening, then:

$$\left(\frac{\partial \tau}{\partial \gamma} \right)_{\dot{\gamma}, \theta} = - \left(\frac{\partial \tau}{\partial \theta} \right)_{\gamma, \dot{\gamma}} \cdot \frac{d\theta}{d\gamma} \quad (2)$$

That is, at $d\tau = 0$ the rate of strain hardening is balanced by thermal softening. Neglecting heat conduction, the adiabatic rate of temperature increase due to the conversion of plastic work to heat is:

$$\frac{d\theta}{d\gamma} = \frac{\beta\tau}{\rho c} \quad (3)$$

where ρ is material mass density, c is specific heat, and β is the fraction of plastic work converted to heat. Based on the work of Taylor & Quinney (1934), β is usually taken to be between 0.85 and 0.95. Taylor and Quinney found that the value of β was material-dependent. More recently, it has been determined that β also depends on strain and strain rate (Mason et al. 1994). Using Equations 2 and 3 and a constitutive relationship between shear stress and shear strain, a critical instability strain for the onset of adiabatic shear can be derived. For a simple form of power-law hardening, $\tau = k\gamma^n$, the instability strain is:

$$\gamma_i = \frac{n\rho c}{-\left(\frac{\partial\tau}{\partial\theta}\right)_{\gamma,\dot{\gamma}}} \quad (4)$$

This expression shows the importance of strain hardening (through the strain hardening exponent, n) and the volumetric heat capacity (ρc) in retarding instability, and of thermal softening ($\partial\tau/\partial\theta$) in accelerating it. Comparable expressions for critical instability strains for a variety of other constitutive relations are given in Table 6.1 of Bai & Dodd (1992).

Along with maximum stress, a number of different adiabatic shear failure criteria have been proposed, including:

- Maximum stress (Zener & Hollomon 1944)
- Critical strain (Bai & Dodd 1992; Batra et al. 1995)
- Kinetic energy change (Shawki 1994a; Shawki 1994b)
- Collapse of shear stress (Wright & Batra 1985)
- Stress intensity factor (Mason et al. 1994b; Zhou et al. 1996; Chen & Batra 1998)

An issue for modeling of adiabatic shear is that defining “failure” by maximum stress or certain other criteria does not necessarily capture the inception of an adiabatic shear band. Rather, instability strain indicates where shear localization begins, which is a precursor to the point at which the intense shear gradients of an adiabatic shear band have formed.

Experimental Procedure and Results

Materials

A range of alloys was chosen for this project, including materials of interest for Sandia applications and those representing a wide range in susceptibility to adiabatic shear. Classes of materials included plain carbon steel, maraging steel, 300-series austenitic and precipitation hardening stainless steel, aluminum alloys, and titanium alloys. 12.7mm (0.5 in.) square bar and 12.7mm and 19.1mm (0.75 in.) diameter round bar were used for specimens. Alloys tested in the as-received condition included AISI 1018 cold rolled steel (CRS), ASTM A36 (AISI 1020) hot rolled steel (HRS), AISI Type 304 austenitic stainless steel, CP Titanium Grade 2 (Mill Anneal), Ti-6Al-4V (Mill Anneal), and aluminum alloys 2024-T351, 6061-T6, and 7075-T6. 18Ni300 maraging steel and PH13-8Mo precipitation hardening stainless steel were received in the solution anneal condition and machined prior to final heat treatment. The maraging steel was then aged at 480°C (900°F), and the PH13-8Mo was aged at 538°C (H1000 heat treat designation). Representative chemical compositions and mechanical properties for the alloys tested are given in Table 1 and Table 2, respectively.

Aluminum Alloys	Al	Si	Fe	Cu	Mn	Mg	Cr	Zn	Ti	
2024-T351	Bal.	.26	.19	4.6	.45	1.66	.07	.15		
6061-T6	Bal.	.58	.17	.20	.01	.8	.08	.02	.01	
7075-T6	Bal.	.11	.12	1.58	.01	2.41	.25	5.55	.01	
Steel Alloys	Fe	C	Cr	Ni	Mo	Co	Mn	Si	Ti	Al
AISI 1018 (CRS)	Bal.	.18					.68	.22		
ASTM A36 (HRS)	Bal.	.16	.05	.1			.62	.15		
18Ni300 Marage	Bal.	.006	.16	18.6	4.7	8.9	.03	.03	.62	.12
AISI 304 SS	Bal.	.022	18.2	9.1	.39		1.6	.5		
PH13-8Mo	Bal.	.03	12.5	8.1	2.2		.07	.04		1.1
Titanium Alloys	Ti	C	Al	V	Fe	O	N			
CP Ti – Grade 2	Bal.	.01			.07	.14	.007			
Ti-6Al-4V	Bal.	.022	6.34	4.2	.21	.17	.031			

Table 1: Chemical Composition of Alloys

Based on physical and mechanical properties and prior investigations (e.g., Timothy 1987), it was expected that 304 stainless steel would be highly resistant to adiabatic shear failure, 6061-T6 aluminum would be moderately resistant, and the remaining alloys would be moderately to highly susceptible.

	Yield Strength	Ultimate Tensile Str.	Elongation	Reduction in Area
	ksi	ksi	pct.	pct.
Aluminum Alloys				
2024-T351	51.7	68.6	12.0	
6061-T6	37.0	40.3	12.8	
7075-T6	79.6	89.2	15.1	
Steel Alloys				
AISI 1018 (CRS)	68	75	22	45
ASTM A36 (HRS)	52.1	71.2	28	
18Ni300 Marage	288.3	299.7	11.0	53.8
AISI 304 SS	81.4	99.9	43.5	72.0
PH13-8Mo (H1000)	208.0	215.8	13.1	57.6
Titanium Alloys				
CP Ti – Grade 2	53.0	77.0	26	54.5
Ti-6Al-4V	144.7	153.9	18.2	47.5

Table 2: Mechanical Properties of Alloys

Specimen Evaluation

A primary objective of this project was the identification or development of an experimental technique that could be used for screening materials for evaluation of high-rate mechanical properties and susceptibility to adiabatic shear. Important attributes of such an experimental technique include:

- Applicable to materials with a wide range in level of susceptibility to adiabatic shear.
- Capable of yielding quantitative data related to deformation behavior and adiabatic shear susceptibility.
- For screening purposes, should not be expensive or difficult to perform.

These requirements are, to a significant extent, mutually incompatible. Difficulties with development of a “universal” screening test include:

- Alloys that are relatively resistant to adiabatic shear banding may require very high strains and/or strain rates to demonstrate susceptibility. High-rate experimental methods that provide good quantitative data for characterizing deformation behavior (e.g., torsional Kolsky bar) are typically limited in maximum achievable strain or strain rate. Thus, they may not be suitable for detecting susceptibility in alloys with moderate to high resistance.
- Alloys that are highly susceptible to adiabatic shear (e.g., those with low work hardening) may also be highly notch-sensitive. As a result, design of the test specimen gage section may be critical to assure that failure occurs as a result of rate-dependent adiabatic shear rather than rate-insensitive notch sensitivity.

- Ballistic penetration and punch-type experiments are very useful for providing qualitative or phenomenological evidence of adiabatic shear in alloys with a wide range of susceptibilities. However, they are generally unable to provide significant quantitative data of the type needed to characterize the onset of adiabatic shear.

Given these considerations, it was decided to initially evaluate two experimental methods: the torsional Kolsky bar, and impact-loaded Double Linear Shear. It was recognized that both methods had apparent limitations on range of applicability, but that they had the capability to provide quantitative data on adiabatic shear susceptibility and (in the case of torsional Kolsky) high-rate deformation behavior. Issues with the performance of these techniques in initial experiments then led to the adoption of a new design, the Shear Compression Specimen, as the principal technique for evaluating dynamic behavior.

Double Linear Shear

The linear shear technique adopted in the early stages of this project was that of Cowie et al. (1989). The specimen is a square doubly-notched bar (Figure 3) whose ends are rigidly clamped while the center section is impacted by a striker. The machined notches on either side of the center section provide a narrow minimum-area gage section where shear deformation localizes. The experiments of Cowie et al. used a pendulum-type impact apparatus to dynamically load 4340 steel specimens.



Figure 3a: Double Linear Shear specimen.

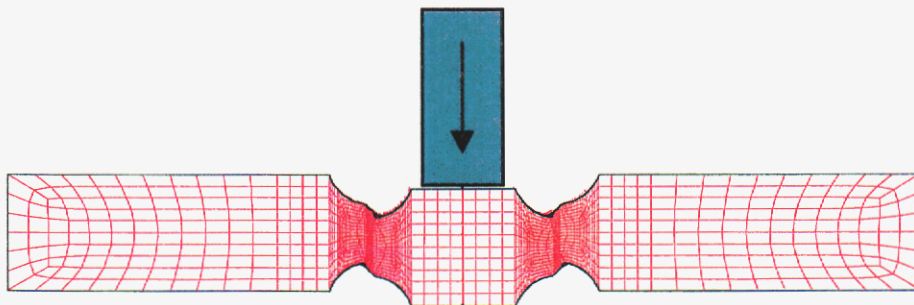


Figure 3b: Finite element simulation of shear deformation in gage sections of Double Linear Shear specimen. Ends of specimen are rigidly clamped, and striker impacts center section.

Our evaluation used a Dynatup® Model 8250 drop-weight impact test system to load the specimens. An important issue with this technique was whether loading rates and impact energies were sufficient to induce adiabatic shear in resistant alloys. Therefore, initial experiments were conducted with 6061-T6 specimens. These tests showed that, while substantial shear deformation and occasional failure in the gage section could be induced with 6061-T6, no evidence of adiabatic shear localization was found. Finite element simulations (for example, Fig. 3) also indicated that shear localization could likely be induced in a susceptible alloy like Ti-6Al-4V, but not in 6061. Given this limitation and the high expense associated with machining the notched gage section in this specimen, no further evaluation of Double Linear Shear as a screening-type test configuration was conducted.

Torsional Kolsky Technique

The torsional Kolsky bar or Torsional Split-Hopkinson Bar (TSHB) has been widely used for characterizing high-rate deformation behavior and adiabatic shear. A thorough discussion of the technique is given in Hartley et al. (1985). Briefly, the test specimen is mounted between an incident-pulse bar and a transmitted-pulse bar, Figure 4.

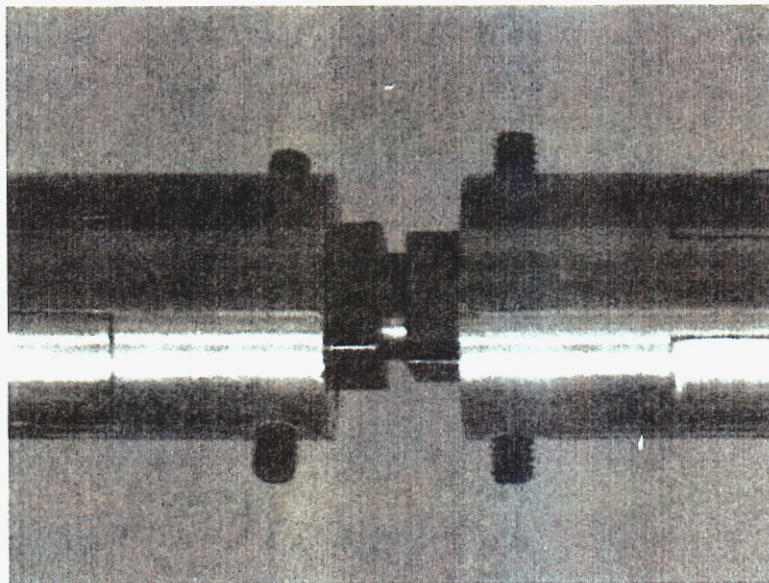


Figure 4: TSHB specimen with straight (90°) shoulders at edges of tubular gage section. Square ends of specimen lock into the incident-pulse bar and transmitted-pulse bar of the torsional Kolsky apparatus. Incident bar has rotated more than one complete revolution in this experiment without causing failure in gage section.

Variations in test parameters allow for testing over a range of strains and strain rates. The specimen gage section is typically a thin-wall tubular design. The specimen is loaded by the sudden release of stored elastic energy that is obtained by initial rotation and then release of the incident bar, while the transmitter bar is kept fixed. A major advantage of the technique is that a direct measure of shear stress and shear strain can be obtained from the output of the strain gages on the incident-pulse and transmitted-pulse bars that load the specimen. Thus, a high-rate shear stress vs. shear strain relationship can be generated. The axisymmetric configuration is also an advantage for modeling and simulation.

An important consideration with the torsional Kolsky bar is that maximum achievable strains and strain rates are limited. The maximum strain rate is approximately 10,000/s, but in practice most data are obtained at rates of 3000/s or lower. Further, in alloys with high strain-to-failure, multiple “hits” may be required to produce sufficient strain to fail the specimen. It was therefore recognized that this technique might not be suitable for evaluating adiabatic shear susceptibility in resistant alloys.

An additional consideration was design of the transition from the thin-wall gage section to the shoulder of the grip area. There are some advantages to a 90° shoulder (see Fig. 4) with a tight radius at the gage-to-shoulder transition. However, for alloys that were anticipated to show notch sensitivity, the high stress concentration with such a transition was considered to be undesirable. Therefore, a modified specimen design with a 45° shoulder was chosen (Figure 5), and the effects of different transition radii were evaluated. The objective was to keep the failure location within the thin (0.4mm) uniform-thickness gage section, rather than at the shoulder. Competing influences are stress concentration, which favors a shoulder failure location, and thermal conduction from the “hot” plastically deforming gage section to the “cool” non-deforming shoulders, which favors a central gage section failure. Conduction becomes less important as strain rate increases.

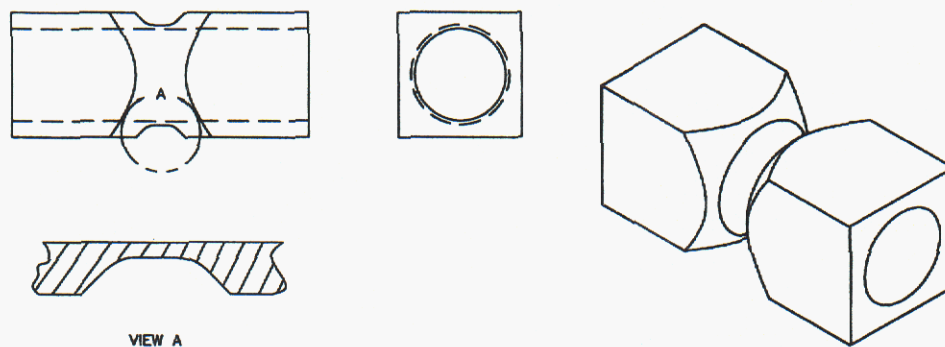


Figure 5: Torsional Kolsky bar specimen with 45° shoulders at edge of gage section (see View A).

With this specimen design, dynamic torsion experiments involving the alloys shown in Table 1 were conducted at the California Institute of Technology (Cal Tech), using the torsional Kolsky apparatus in their Graduate Aeronautical Laboratories. These screening

experiments showed that failure in a single “hit” could only be obtained for alloys with low strain-to-failure; higher ductility alloys required multiple reloadings. Failure by adiabatic shear appeared to occur in a few cases, but metallographic confirmation was difficult to obtain.

Metallographic investigation of shear failures in this specimen is made difficult by the required orientation of the sectioning plane; it must pass through the thin direction of the gage section in order to show axial strain gradients at the failure plane, which is normal to the specimen axis. In addition, where failure occurs there is rubbing of the two failure surfaces that produces a near-surface shear deformation, one that is difficult to distinguish from adiabatic shear. An example where metallography disclosed an incipient shear localization failure is shown in Figure 6. In this unfailed 2024-T3 specimen, uniform shear and shear localization in the gage section are indicated in an etched metallographic cross-section by the orientation of precipitates. Pre-test they were oriented axially in the specimen, while post-test they are oriented at a constant angle across the entire gage section, with local sharp discontinuities in orientation plus a small shear crack. The constant angle orientation is indicative of uniform strain in the gage section, while the discontinuities and shear crack indicate localization that is likely just short of the onset of adiabatic shear failure.

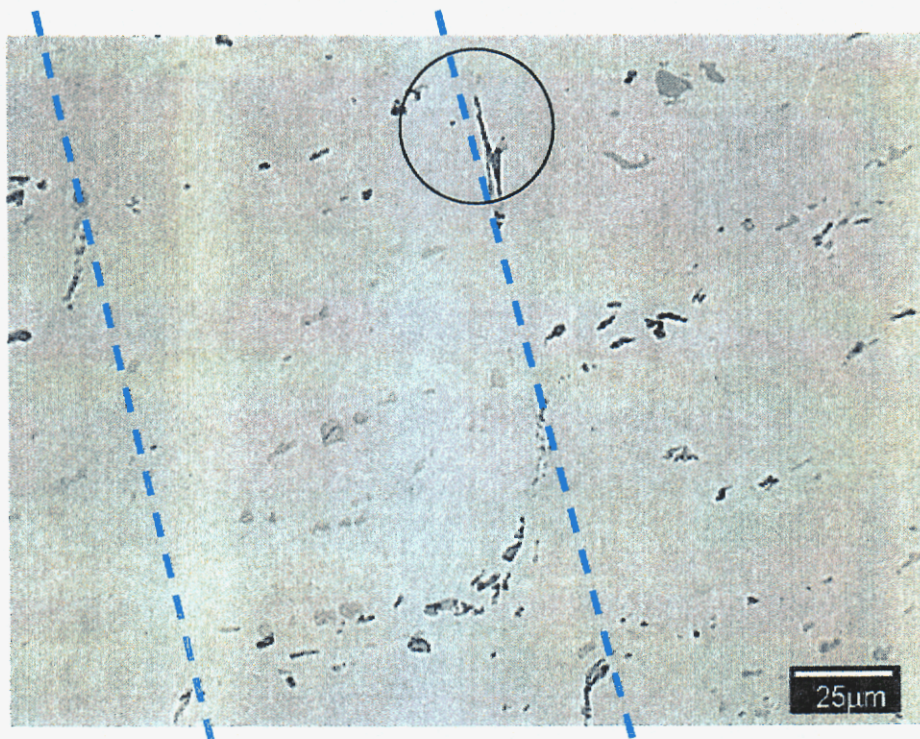


Figure 6: Metallographic cross-section of 2024-T3 aluminum torsional Kolsky specimen showing shear localization (dotted lines) and shear crack (circle). General $\sim 25^\circ$ slope of precipitates indicates uniform shear strain; sharp shear discontinuity and shear crack indicate incipient shear bands.

The torsional Kolsky technique remains a very useful technique (within strain rate limitations) for evaluation of high-rate deformation behavior short of failure. However, the present screening experiments disclosed two major problems with its use for evaluating susceptibility to adiabatic shear. First, inherent limitations on achievable strains and strain rates precluded use with a number of the alloys included with this investigation. Second, it was determined that the strain at apparent failure was too closely tied to the machined surface finish in the gage section. Given the small thickness (0.4 mm, or 0.015 in.) of the tubular gage section, expected thickness variations are likely to be significant in an “affordable” specimen for screening tests, due to machining variations. In high-rate shear, these essentially uncontrolled variations likely serve as the triggering defect for the initiation of adiabatic shear. The likelihood that they will trigger premature localization becomes higher as their size as a percentage of wall thickness increases. The issue of defects and stress concentrations as triggering sites was mentioned previously (Wright 1994; Batra et al. 1996).

Despite perceived drawbacks with the torsional Kolsky as an experimental technique for this application, it has been retained here for some modeling and simulation studies due to the simplicity of its axisymmetry.

Shear Compression Specimen

In an effort to alleviate some of the drawbacks experienced with the torsional Kolsky technique, the Shear Compression Specimen (SCS) was adopted. This is a new type of impact-loaded specimen (Rittel et al. 2002a), which has a reduced gage section at an angle to the loading axis (Figures 7 and 8).

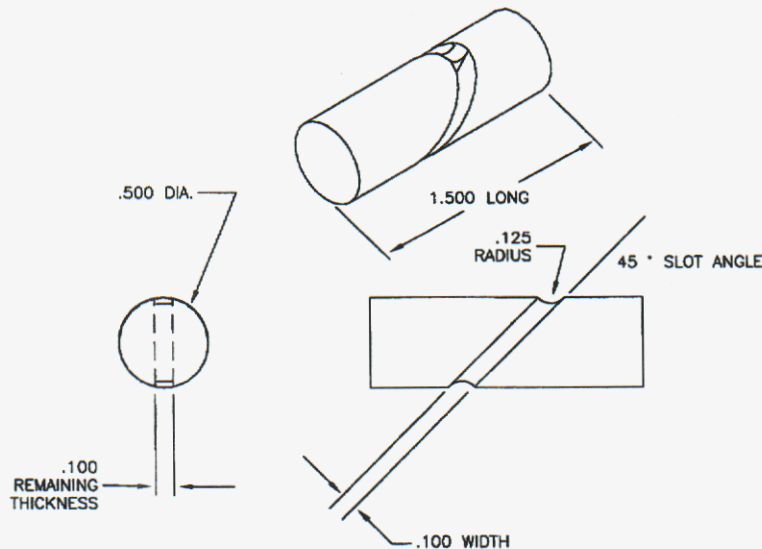


Figure 7: Original design for Shear Compression Specimen (SCS). Height-to-diameter ratio is 3.0, and slot width is 2.5 mm (0.100 in.). A 0.125 in. radius groove is machined where the slot gage section reaches the outside diameter of the specimen.

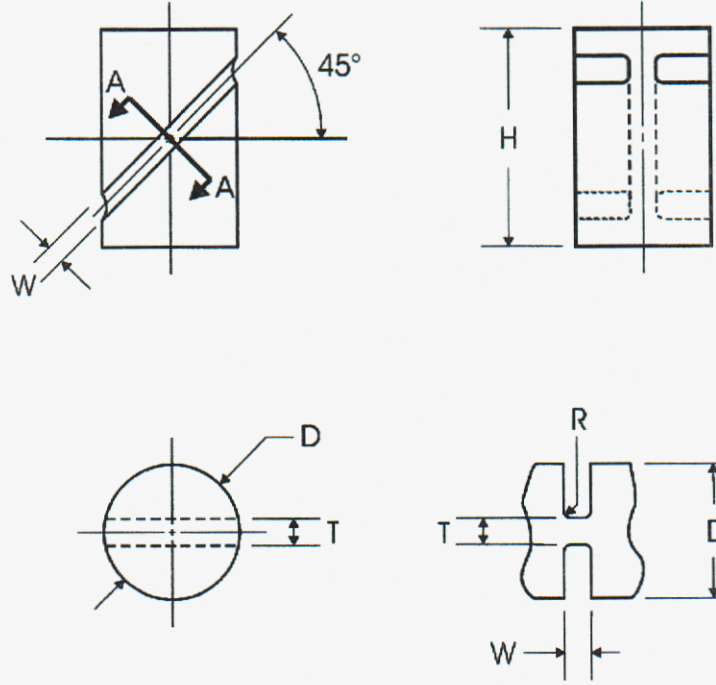


Figure 8: Modified SCS design with H/D ratio of 1.6. Specimens with diameters (D) of 7.6 mm and 12.7 mm and slot widths (W) of 2.4 mm, 1.6 mm, 0.5 mm, and 0.25 mm were tested.

The short cylindrical specimen is loaded in compression, which produces a shear-compression stress state in the angled gage section. The ratio of shear to compression is governed by the angle of the diametrically-opposed slots or notches, which to date has been maintained at 45°. Although the stress and strain state in the gage section is three-dimensional, at this angle the dominant deformation mode is shear.

The cylindrical sections above and below the gage section of the SCS specimen are assumed to remain elastic. Analysis and experiments (see Figure 9) establish that this assumption is correct. Finite element analysis was used to determine numerically the stress and strain states in the specimen, and to develop a constitutive law relating the nominal equivalent stress (σ_{eq}), plastic strain (ϵ_{eq}), and plastic strain rate ($\dot{\epsilon}_{eq}$) in the gage section in terms of relevant SCS geometrical parameters and the boundary displacement and load (Rittel et al. 2002a). The following relations have been proposed:

$$\epsilon_{eq} = \frac{d}{W} \quad (5)$$

$$\dot{\epsilon}_{eq} = \frac{\dot{d}}{W} \quad (6)$$

$$\sigma_{eq} = 0.85(1 - 0.2\epsilon_{eq}) \frac{P}{DT} \quad (7)$$

where (see Fig. 8) W is slot width, D is specimen diameter, T is gage section thickness, and P , d , and \dot{d} are boundary load, displacement, and displacement rate, respectively.

Specimens may be loaded quasi-statically in conventional screw-driven or servo-hydraulic machines, or dynamically in compression Split-Hopkinson Pressure Bar apparatus. Equation 6 shows that strain rate depends on both loading rate and width of the machined slot. This facilitates testing at a wide range of strain rates. Of particular advantage, by testing specimens with varying slot widths in both conventional-rate and high-rate apparatus, the entire strain rate range up to 10,000/s or higher can be covered by a single technique. Further, by testing narrow-slot SCS specimens dynamically, strain rates can be achieved that are far higher than those possible with compression SHPB testing of cylindrical specimens. The relatively large thickness of the SCS gage section (T) also means that expected periodic or random variations in thickness due to machining processes will have a lesser effect than they would for a thin gage section, such as occurs for torsional Kolsky specimens.

Initial SCS specimens for this project were of the type shown in Figure 7, with a diameter of 12.7 mm (0.5 in.) and a height-to-diameter ratio of $H/D = 3.0$. This H/D ratio was chosen initially to assure that boundary conditions at the specimen ends would not adversely influence behavior in the gage section. Subsequent modeling and experiments (e.g., Figure 9) disclosed that the specimen gage section was well behaved at significantly lower H/D , and a H/D ratio of 1.6 was therefore used for most experiments (Figure 8).

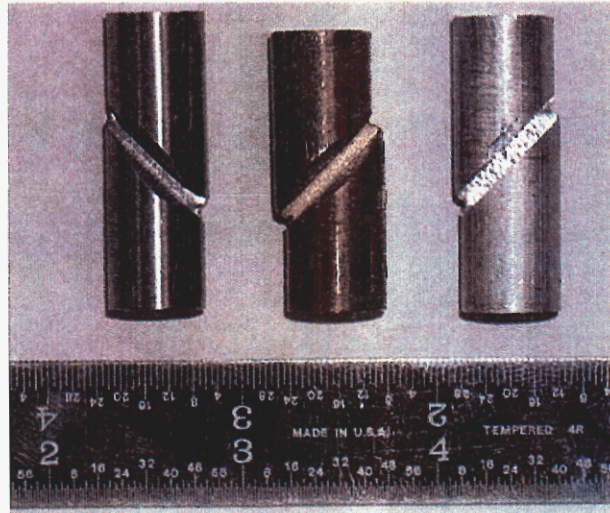


Figure 9: SCS specimens ($H/D = 3$) showing lateral displacement due to shear deformation in the gage section. Materials are Ti-6Al-4V (left), OFHC copper (center), and 6061-T6 aluminum (right).

OFHC copper specimens were used during initial development of the SCS geometry {Rittel et al. 2002a; Rittel, et al. 2002b), so that very high shear strains could be obtained without failure. For the current project, specimens were made from 1018 cold rolled steel, A36 hot rolled steel, 18Ni300 Marage steel, 2024-T3, 6061-T6, 7075-T6, CP Titanium, and Ti-6Al-4V. For most SCS specimens, H/D was 1.6 with $H = 20.3$ mm (0.8 in.) and $W = 12.7$ mm (0.5 in.). Some 20.3 mm-tall specimens were also tested that had $D = 7.6$ mm.

In all specimens, the thickness of the gage section (T) was 2.5 mm (0.100 in.). Baseline slot width (W) for the SCS specimens was 2.4 mm (0.094 in.). Other slot widths tested for some alloys were 1.6 mm (0.063 in.), 0.5 mm (0.020 in.), and 0.25 mm (0.010 in.). Specimens with this range of slot widths are shown in Figure 10.

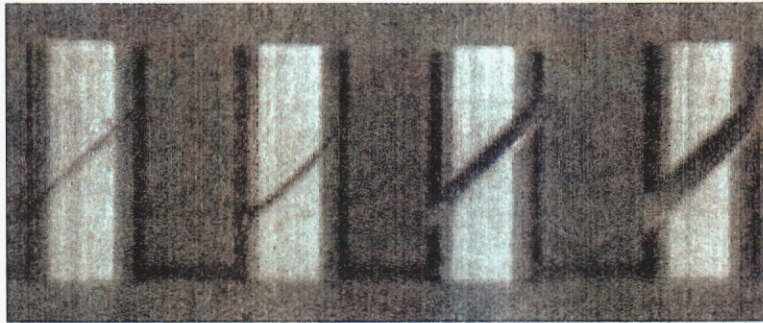


Figure 10: Variation in slot width for SCS specimens ($H/D = 1.6$). From left to right, slot widths are 0.25 mm, 0.50 mm, 1.6 mm, and 2.4 mm.

Nominal root corner radius R (Fig. 8) was 0.25 mm, but a limited number of specimens were tested to evaluate the effect of a tighter (0.13 mm) corner radius. No effect was seen for this range, so the 0.25 mm radius was adopted to simplify machining. Other variations included the presence or absence of an end groove in the gage section where it intersects the specimen outside diameter. In Figure 7 an end groove is shown with a 0.125-in. radius. The initial purpose was to reduce a predicted stress concentration at this point. Figures presented in the following section contain data for specimens with and without the end groove. Since the data show that there is no apparent difference in behavior, the end groove is no longer specified.

SCS specimens were tested at Cal Tech using an Instron screw-driven machine to achieve lower strain rates, and SHPB apparatus for higher strain rates. The maximum rate for the Instron machine is 550 mm/min; for this displacement rate, the maximum strain rate is 23/s in the gage section of an SCS specimen with a gage width of 0.25 mm. Using a 0.25 mm gage width and the dynamic SHPB apparatus, maximum strain rates up to 70,000/s were possible.

In the initial evaluation of the SCS specimen with OFHC copper, companion high-rate experiments were performed on Instron and the SHPB apparatus using conventional cylindrical “Hoppy bar” specimens. The purpose was to verify that properties measured with the SCS specimen corresponded to values measured at similar strain rates using accepted quasi-static (screw-driven) and dynamic (compression SHPB) techniques and

cylindrical specimens. The same comparison was done in this project for 1018 cold rolled steel and 6061-T6 aluminum. Cylindrical specimens tested here were 7.62 mm diameter and lengths 7.62 mm, 3.81 mm, and 1.90 mm (L/D of 1.0, 0.5, and 0.25).

SCS Experimental Results: Shear Deformation and Failure

SCS experimental results for rate effects on deformation behavior are shown in Figures 11-20. Data are plotted as equivalent flow stress at 10% equivalent plastic strain vs. strain rate. Equivalent stress is chosen to facilitate comparison with compression data for cylindrical specimens. 10% strain represents a level at which data oscillations inherent in dynamic data have damped out, and strain rate effects on flow properties are apparent.

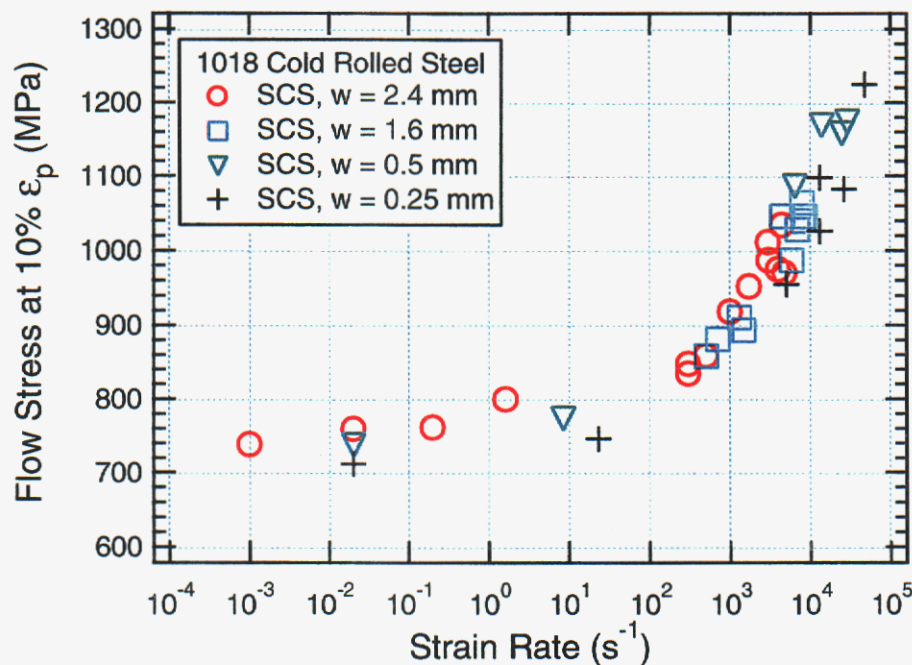


Figure 11: Effect of strain rate on flow stress for 1018 cold rolled steel. SCS specimens with slot widths from 0.25 mm to 2.4 mm.

Figures 11 to 13 show data for experiments conducted on 1018 steel, in which much of the evaluation of the SCS specimen design was concentrated. SCS-only data are shown in Figure 11, cylindrical SHPB-only in Figure 12, and combined data in Figure 13. Data for four different SCS slot widths are shown in Figure 13. Instron-based data at rates of 23/s and lower show a relatively small strain rate dependence, while dynamic SCS data at rates above 100/s show the expected much-higher rate dependence associated with a change in rate-dependent deformation mechanism from dislocation glide resistance to phonon drag (Sargent & Ashby 1983). The maximum rate achieved with dynamic testing of the 0.25 mm slot width was 47,000/s. There appears to be no strong consistent effect of slot width over the range 0.25 mm to 2.5 mm, although narrow-slot data are typically somewhat lower than wide-slot data.

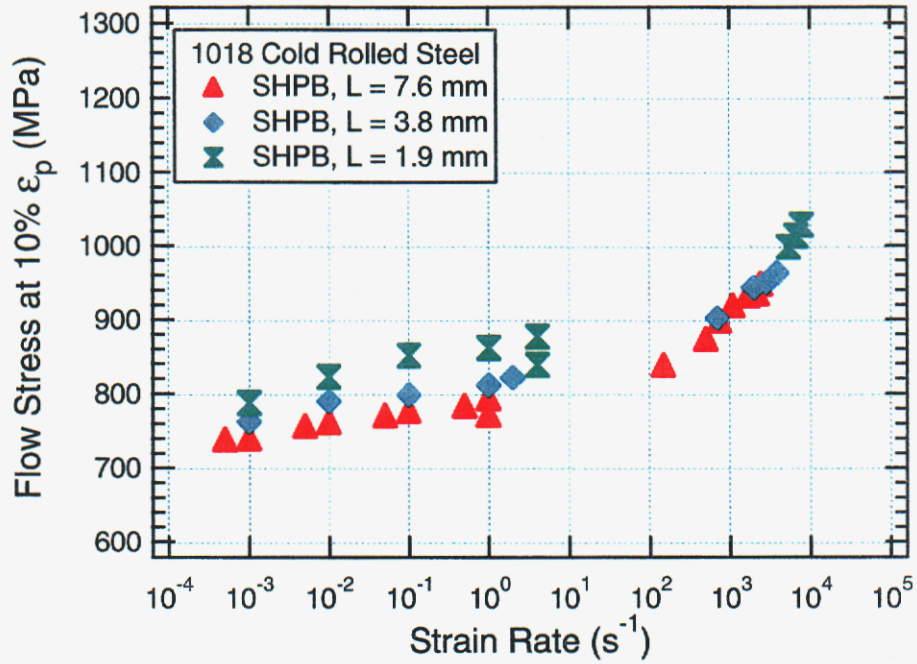


Figure 12: Effect of strain rate on flow stress for 1018 cold rolled steel. Cylindrical specimens with diameter of 7.6 mm and height varying from 1.9 mm to 7.6 mm.

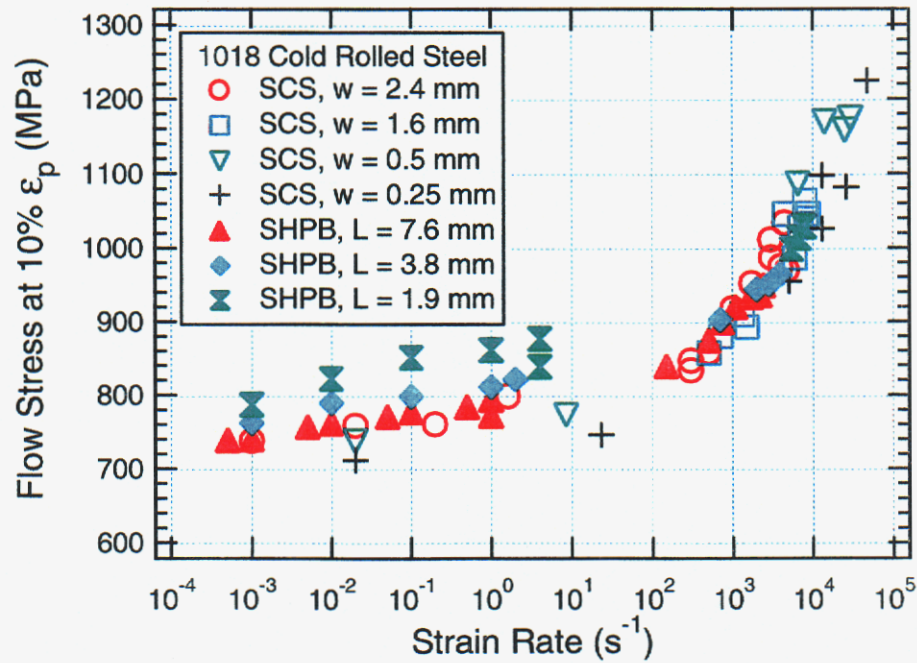


Figure 13: Effect of strain rate on flow stress for 1018 cold rolled steel. Comparison of SCS specimens and cylindrical compression specimens.

The same trends in strain rate effects on flow stress are seen with the 1018 steel cylindrical specimen data in Figure 12. However, here a size effect (or geometry effect) is apparent at quasi-static rates, where short specimens give higher flow stress values than conventional $L/D = 1$ specimens. This is attributed to the greater relative effect of friction in short specimens where the frictional surface-to-volume ratio is high. The combined data are shown in Figure 13. There is excellent agreement between SCS cylindrical specimen data at dynamic rates. At quasi-static rates there is also good agreement between SCS data (particularly wide-slot data) and cylindrical specimen data for $L/D = 1$.

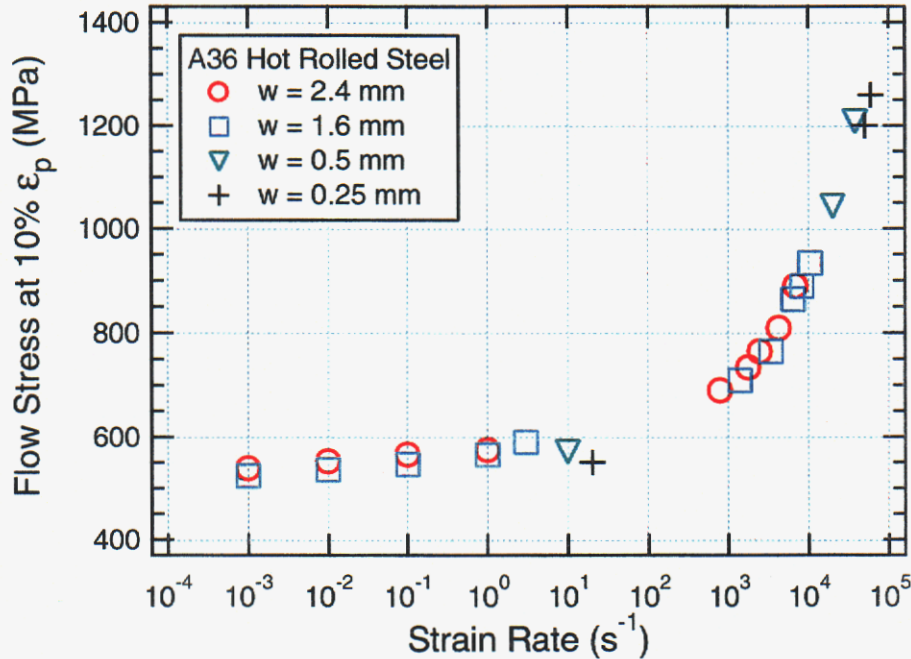


Figure 14: Effect of strain rate on flow stress for A36 hot rolled steel. SCS specimens with slot widths from 0.25 mm to 2.4 mm.

SCS data for A36 hot rolled steel are shown in Figure 14 for four different slot widths. There is no apparent effect of slot width for dynamic tests, and only a slight effect at quasi-static rates. As with the 1018 steel results, flow stress values for narrow slot widths are slightly lower than those for the baseline 2.4 mm width. There is a small rate dependence of flow stress at rates below 20/s, and the expected increase in rate dependence for strain rates of 1000/s and above. The maximum strain rate was 60,000/s.

The two largest slot widths, 2.4 mm and 1.6 mm, were evaluated for 18Ni300 Maraging steel (Figure 15), CP Titanium (Figure 16), and Ti-6Al-4V (Figure 17). The effect of end grooves was also evaluated with the two titanium alloys. The maraging steel shows at small rate dependence of flow stress at lower strain rates, while the effect is much stronger for the titanium alloys. As in 1018 and A36 steel, there is an indication that measured values of flow stress are somewhat lower for SCS specimens with the more narrow slot width. Comparing data for titanium alloy specimens with and without end grooves, there is no significant difference in results at the dynamic rates where the

comparison was made. Maximum strain rates for SCS specimens with these alloys were in the range 6500 to 11,000/s.

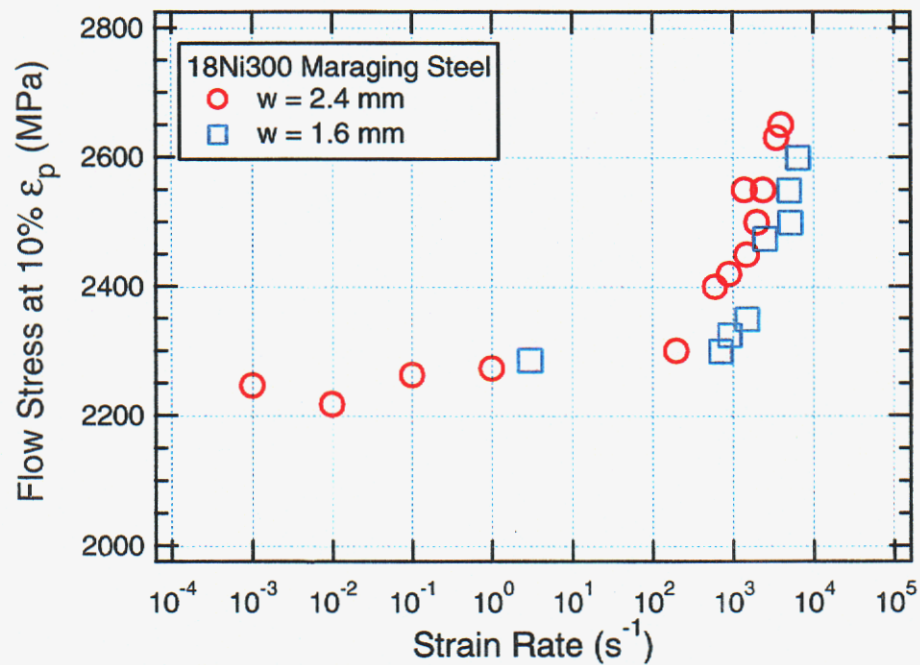


Figure 15: Effect of strain rate on flow stress for 18Ni300 Maraging steel. SCS specimens with slot widths of 1.6 mm and 2.4 mm.

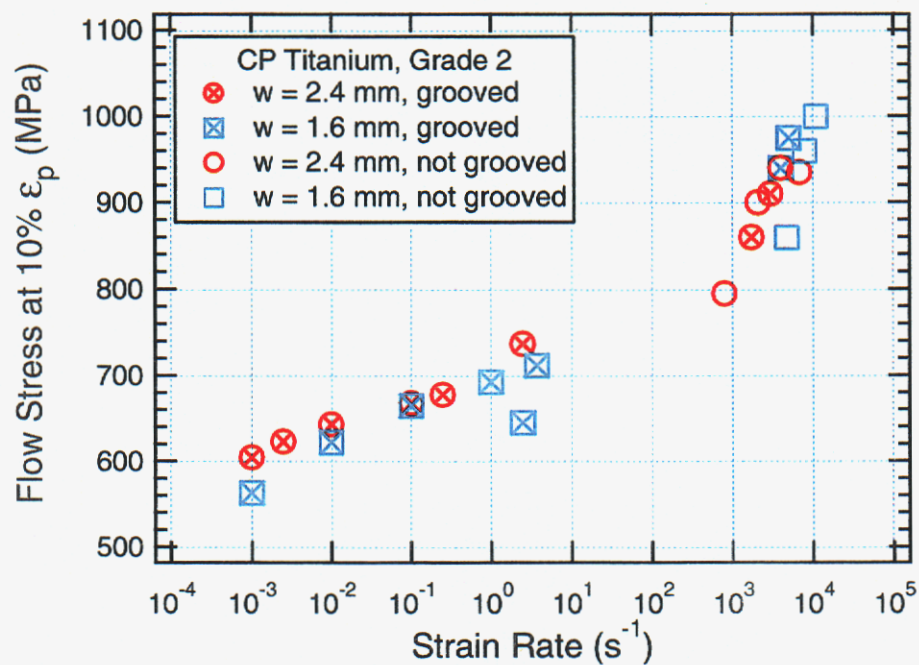


Figure 16: Effect of strain rate on flow stress for CP Titanium Grade 2. SCS specimens with slot widths of 1.6 mm and 2.4 mm, with and without end grooves.

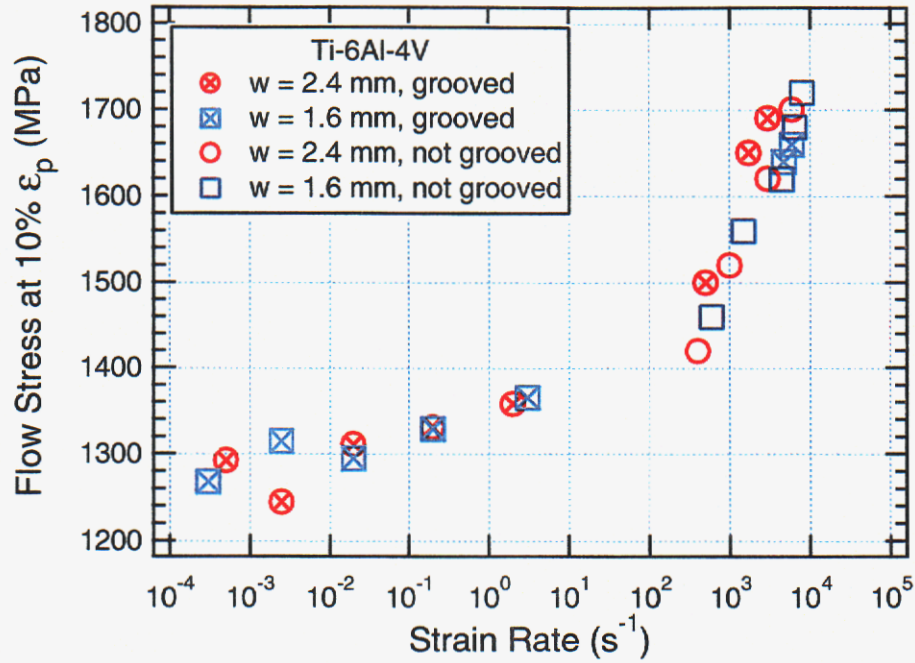


Figure 17: Effect of strain rate on flow stress for Ti-6Al-4V. SCS specimens with slot widths of 1.6 mm and 2.4 mm, with and without end grooves.

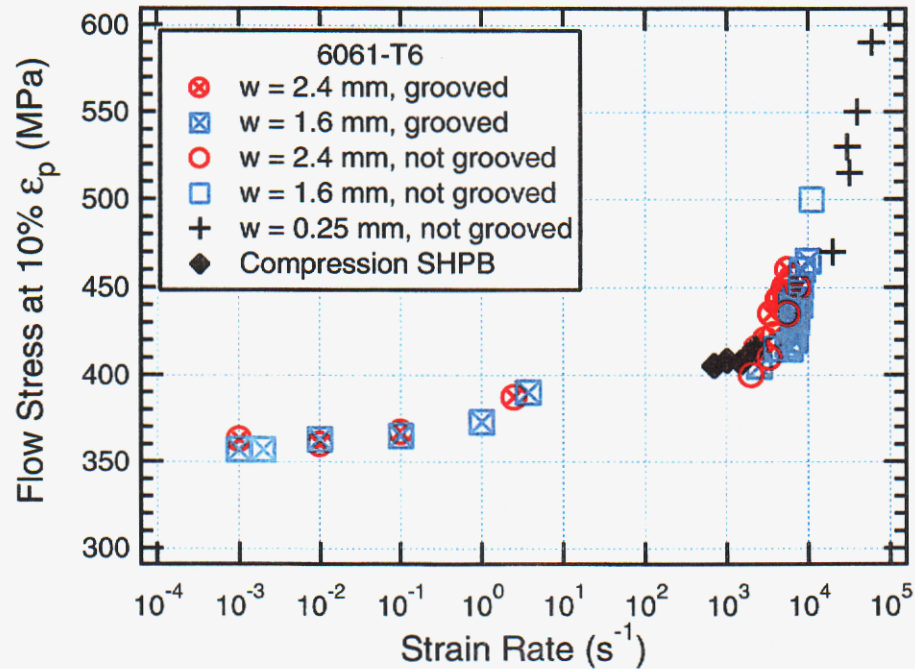


Figure 18: Effect of strain rate on flow stress for 6061-T6 aluminum. SCS specimens with slot widths of 1.6 mm and 2.4 mm, with and without end grooves, compared with cylindrical compression SHPB specimens.

Evaluations of slot width effects, end groove effects, and comparison to cylindrical SHPB results are shown in Figure 18 for 6061-T6 aluminum. The alloy exhibits a small rate dependence at lower strain rates, and again shows the SCS specimens with narrow slots yield slightly lower flow stress values than the baseline 2.5 mm slot width. As with the titanium alloy specimens, presence of an end groove has no apparent effect on performance at dynamic rates. Dynamic SCS results show good agreement with cylindrical SHPB data at strain rates near 1000/s.

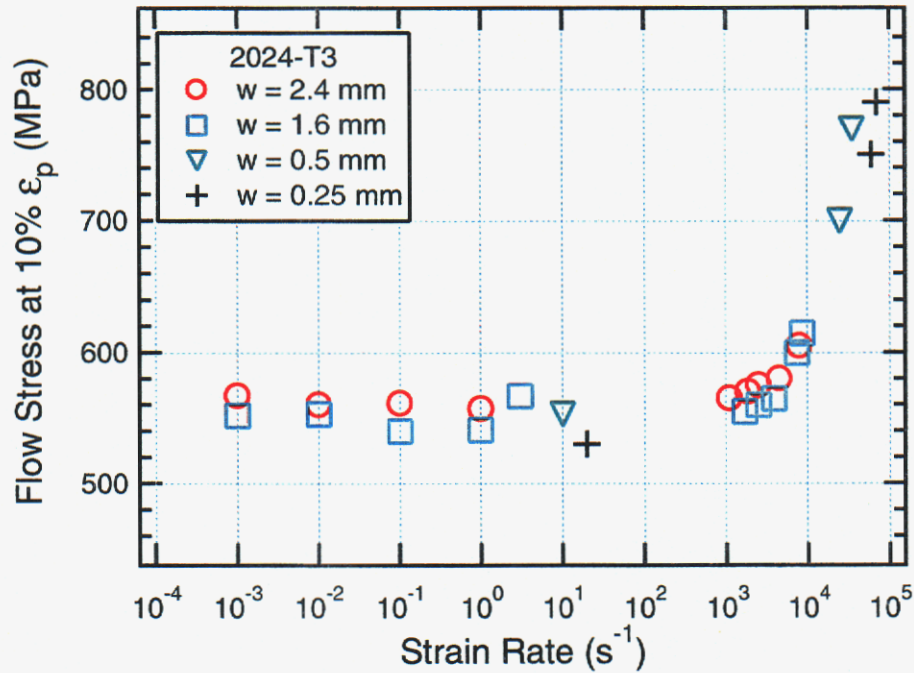


Figure 19: Effect of strain rate on flow stress for 2024-T3 aluminum. SCS specimens with slot widths from 0.5 mm to 2.4 mm.

Both 2024-T3 (Figure 19) and 7075-T6 (Figure 20) appear to be rate-insensitive at quasi-static strain rates. End grooves in 7075-T6 SCS specimens have little apparent effect on dynamic performance. As in all other cases, flow stress values for narrow-groove specimens are typically lower. Maximum strain rates for the three aluminum alloys were from 60,000 to 70,000/s.

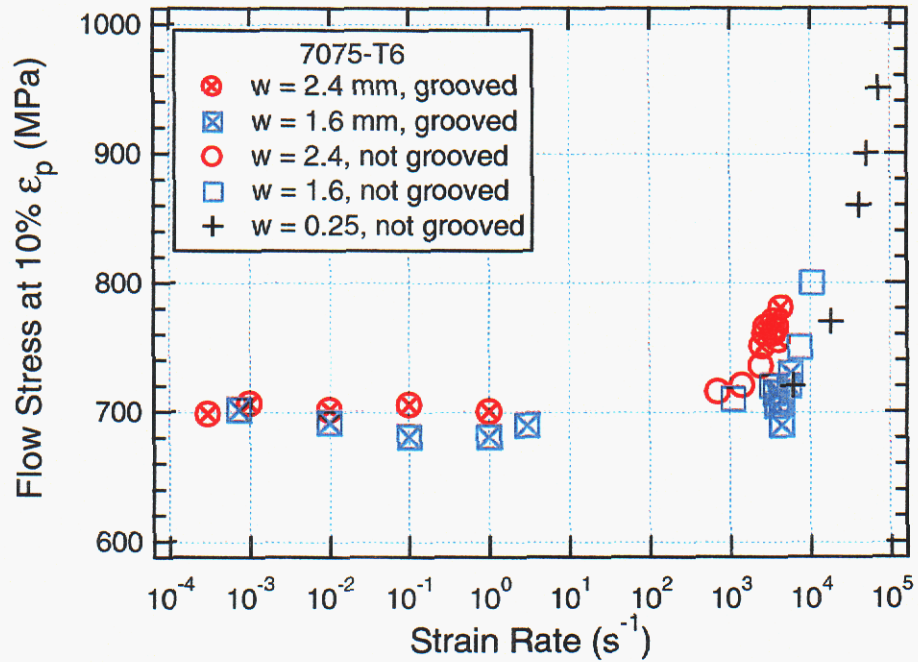


Figure 20: Effect of strain rate on flow stress for 7075-T6 aluminum. SCS specimens with slot widths from 0.5 mm to 2.4 mm, with and without end grooves .

Shear failure did not occur in resistant alloys (6061-T6, A36 steel) except when multiple impacts were performed. In a further effort to induce failure in a 6061-T6 specimen, a narrow slot was EDM machined into the grooved end of the gage section. After dynamic loading at 5500/s, a shear crack was induced to extend a short distance from the end of the EDM slot. However, the loading rate was insufficient to cause complete failure. A metallographic cross-section (Figure 21) shows evidence of shear localization in the gage section at and beyond the end of the shear crack, but the localization appears too diffuse to be considered adiabatic shear.



Figure 21a: Metallographic section showing non-adiabatic shear localization in gage section beyond end of shear crack induced in 6061-T6 by an EDM slot in the gage section.

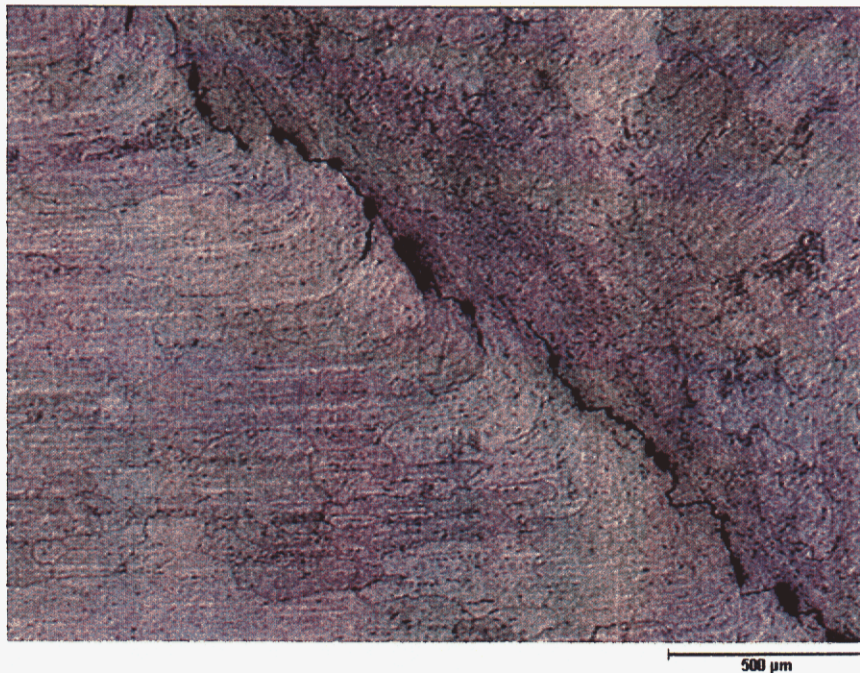


Figure 21b: Non-adiabatic shear localization in gage section at the end of shear crack induced in 6061-T6 by an EDM slot in the gage section. Gage section lower left, undeformed shoulder upper right.

Shear failures were seen in 7075-T6 aluminum and Ti-6Al-4V for strain rates above 3000/s, in CP Titanium for rates above 4000/s, and in 1018 steel and Maraging steel for rates above 5000/s. Clear metallographic evidence of adiabatic shear is seen at the failure surface in Maraging steel. Figure 22 shows white-etching transformed bands both at and below the surface.

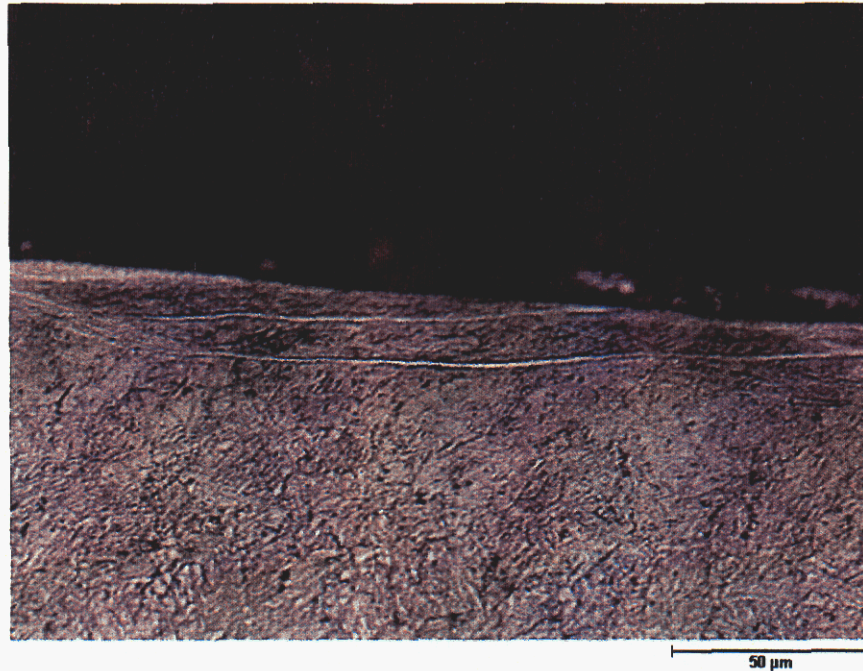


Figure 22: White-etching adiabatic shear bands at and near the fracture surface for an 18Ni300 Maraging steel SCS specimen tested at a strain rate of 5000 per sec. Metallographic section, nital etch.

Metallographic evidence of adiabatic shear banding is more ambiguous for 1018 steel. Figures 23 and 24 show cross sections through the gage section of a specimen that failed at a strain rate of 8000/s (Fig. 23) and one that did not fail at a rate of 4000/s (Fig. 24). In both cases there is non-uniform shear deformation across the width of the gage section, as well as a sharp gradient in deformation at the interface between the edge of the gage section and the undeformed shoulders. The shear localization occurs at the gage/shoulder interface both where failure occurred at this interface (the lower side in Figure 23a) and where it did not (the upper side in Fig. 23a, and both sides of the gage section in Fig. 24a). At higher magnification, shear localization at the gage/shoulder interface is intense and narrow, but it is not of the white-etching transformation type of adiabatic shear band.

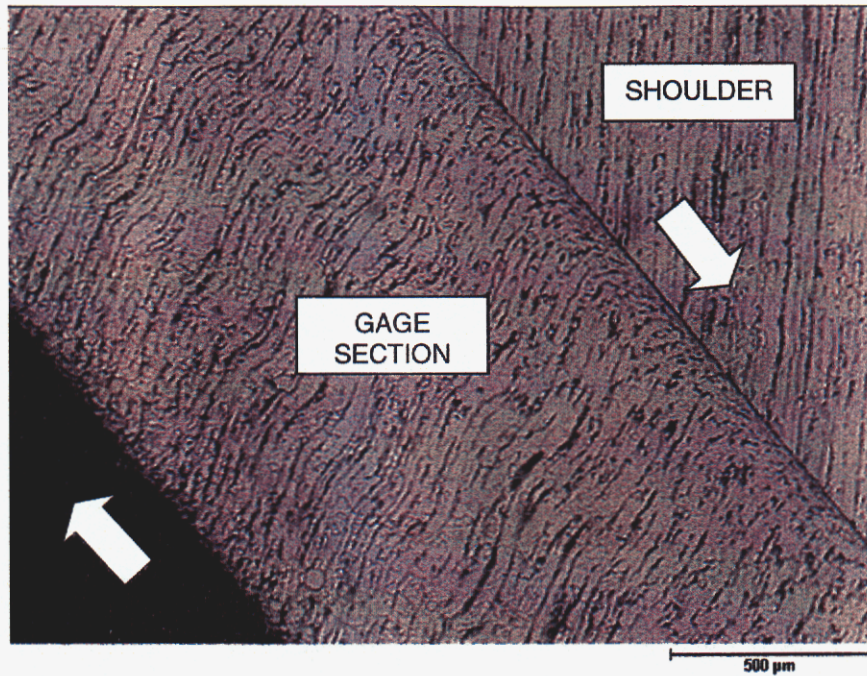


Figure 23a: Metallographic cross-section through gage section of 1018 steel SCS specimen that failed at 8000 per sec. Arrows show shear directions for undeforming shoulders.

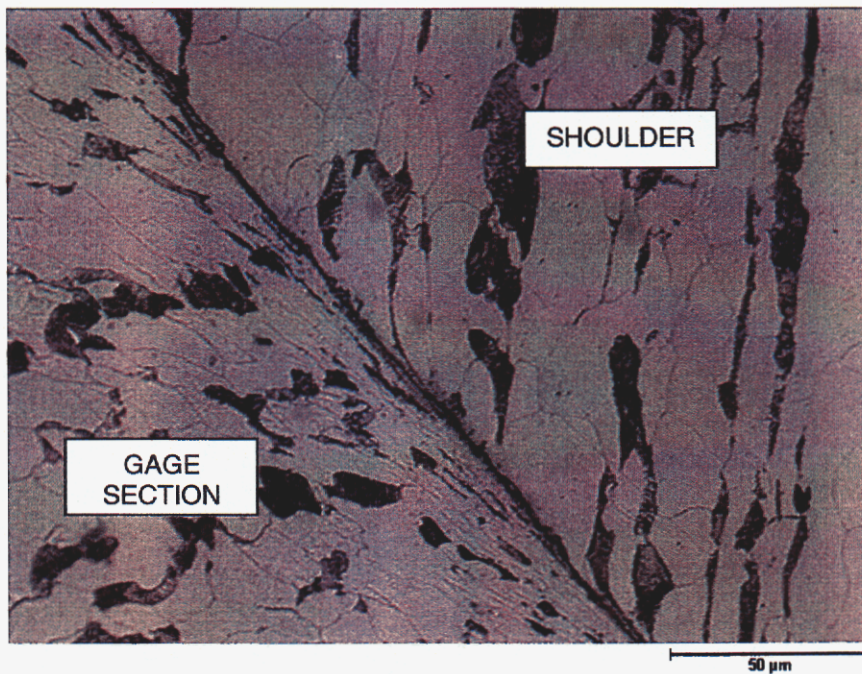


Figure 23b: Higher magnification view of shear deformation at interface between gage section and shoulder.

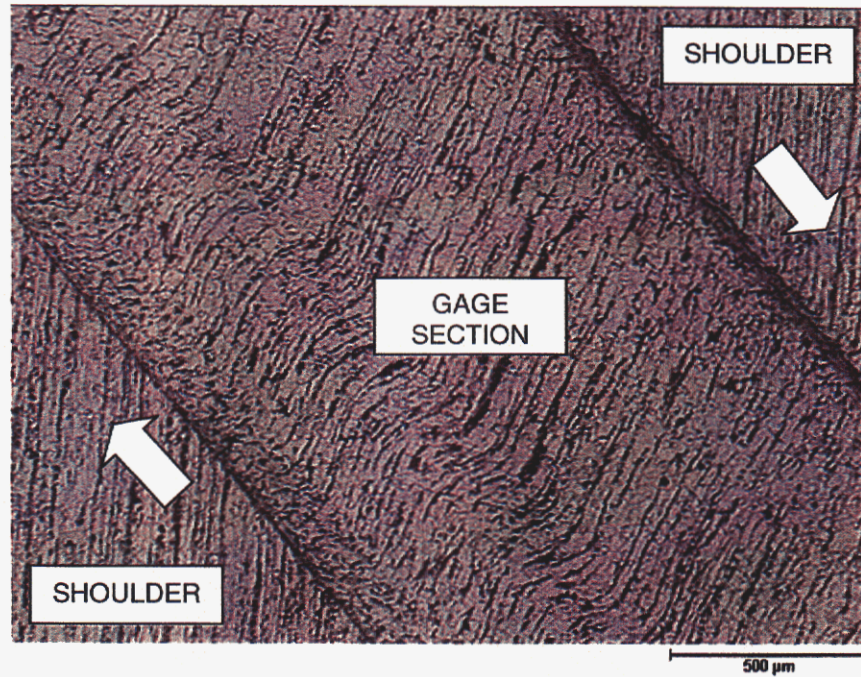


Figure 24a: Metallographic cross-section through gage section of 1018 steel SCS specimen that did not fail at 4000 per sec. Arrows show shear directions for undeforming shoulders.

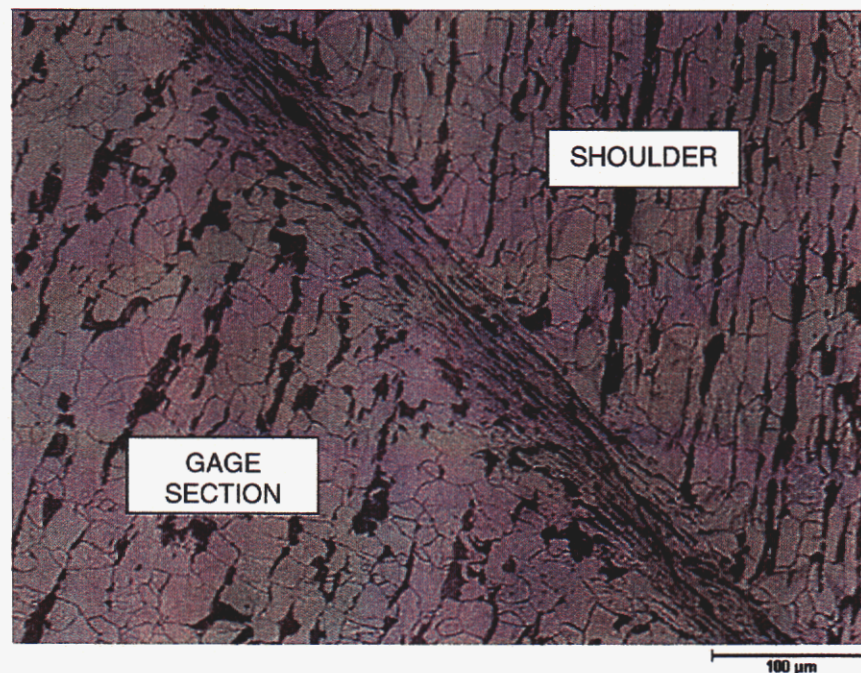


Figure 24b: Higher magnification view of shear deformation at interface between gage section and upper shoulder.

For both quasi-static and dynamic SCS experiments, shear failure (when it occurred) appeared to initiate at the ends of the gage section and propagate toward the middle. While the initial shear failure typically initiated toward the gage section centerline, the fracture path then shifted toward the shoulder (edge of the gage section) in most cases. Variations in radius at the root of the gage/shoulder intersection had no apparent effect on whether a shear failure would run along the edge of the gage section.

Shear failures of this type were seen in some specimens (for example, CP Titanium) at quasi-static as well as dynamic loading rates. As also noted earlier for torsional Kolsky specimens, when macroscopic shear failure occurred the rubbing between the two faces of the failure produced near-surface localized shear deformation that became difficult to distinguish from localized shear that might be attributable to adiabatic shear. That is, in a post-test metallographic examination of a failed specimen it is not clear whether shear localization that preceded adiabatic shear failure can be distinguished from surface shear localization due to post-failure rubbing of the fracture faces. Nevertheless, in 1018 steel and maraging steel it was possible to observe evidence indicating that adiabatic shear localization had probably occurred.

Aside from metallographic evidence that shear localization and shear failure are due to adiabatic shear, observation of a sudden and sharp drop in stress ("stress collapse") may also be taken as possible evidence of adiabatic shear failure. However, SCS specimens do not generally appear to show a rapid stress collapse. In the absence of clear evidence from either metallography or the stress vs. strain record, it is therefore difficult to determine unambiguously whether and at what point an adiabatic shear band has initiated.

Modeling and Simulation

A principal objective of this project was to experimentally determine susceptibility criteria for adiabatic shear failure in alloys of interest to Sandia, which entailed understanding the material state at the inception of adiabatic shear banding. Modeling and simulation, along with microstructural characterization, can aid in this understanding, but may require modeling the actual formation of adiabatic shear bands in order to model their inception; the physical transition between inception and actual formation of adiabatic shear still needs to be experimentally characterized. There are a number of adiabatic shear band constitutive models in the literature that can guide a modeling effort for adiabatic shear failure.

Modeling and simulation for this project had two objectives: 1) conduct simulations using Pronto3D and the BCJ model (Bammann 1990; Bammann et al. 1996) to aid in the design of an experimental specimen that demonstrates adiabatic shear failure in a variety of metals in a repeatable manner; and 2) begin researching a physically-based nonlocal adiabatic shear band constitutive model that captures the formation and propagation of adiabatic shear failure in a mesh-independent manner.

Adiabatic Temperature Evolution

To improve predictions of plasticity-induced heating at high strain rates, a modified adiabatic temperature evolution equation was implemented in Pronto3D. This equation more accurately represents the conversion of plastic work to heat than the classical Taylor & Quinney (1934) assumption that 90% of plastic work is converted to heat under adiabatic conditions. In the modified relationship, the balance of energy density rate assuming adiabatic conditions is:

$$\rho c \dot{\theta} = \sigma : d^p - \kappa \dot{\epsilon}_{ss} \quad (8)$$

where ρ , c , and θ are as described previously, σ is Cauchy stress, d^p is plastic deformation rate, κ is isotropic hardening variable, and ϵ_{ss} is the elastic strain due to statistically-stored dislocations. The adiabatic temperature evolution equation then becomes:

$$\dot{\theta} = \frac{1}{\rho c} \left[\sigma : d^p - \frac{\kappa \dot{\kappa}}{\tilde{c} \mu} \right] \quad (9)$$

where \tilde{c} is a constant and μ is the shear modulus. Integrating the temperature evolution equation using the radial return method and closed form expression leads to:

$$\theta_{n+1} = \theta_n + \frac{1}{\rho c} \left[\sigma_{n+1} : \left(\Delta \gamma \frac{\xi^{trial}}{\|\xi^{trial}\|} \right) - \frac{1}{2\tilde{c}\mu} (\kappa_{n+1}^2 - \kappa_n^2) \right] \quad (10)$$

where ξ^{trial} is the trial effective stress, and $\Delta \gamma$ is the increment of the magnitude of the plastic deformation tensor.

Simulation of Torsional Kolsky and SCS Specimens

Geometric inhomogeneities were incorporated in a 6061-T6 aluminum SCS specimen mesh and in a Ti-6Al-4V torsional Kolsky specimen mesh in order to trigger localized deformation, and simulations were run to understand how the experimental specimen might behave. Although experimental efforts have concentrated on the SCS specimen geometry, the axisymmetric character of the torsional Kolsky specimen makes it attractive for simulations.

For 6061-T6, a machined-in defect in the SCS specimen did not trigger localized deformation in either the experiment (the EDM slot) or the simulation. Conversely, a meshed defect on the order of machining dimensional tolerance in a Ti-6Al-4V torsional Kolsky specimen generated localized deformation that was mesh-dependent (i.e., different shear band thickness and force-displacement plot for each refined mesh). The

experimental Ti-6Al-4V torsional Kolsky also failed due to adiabatic shear, most likely as a result of slight machining surface defects on the thin walls.

For the 6061-T6 SCS specimen, no shear banding was observed in simulations as plastic deformation became concentrated in the fillet regions. Figure 25 shows the deformed mesh at the end of loading. There was significant plastic deformation in the fillet regions but not to the extent that deformation becomes localized and there was a drop in load-carrying capacity.

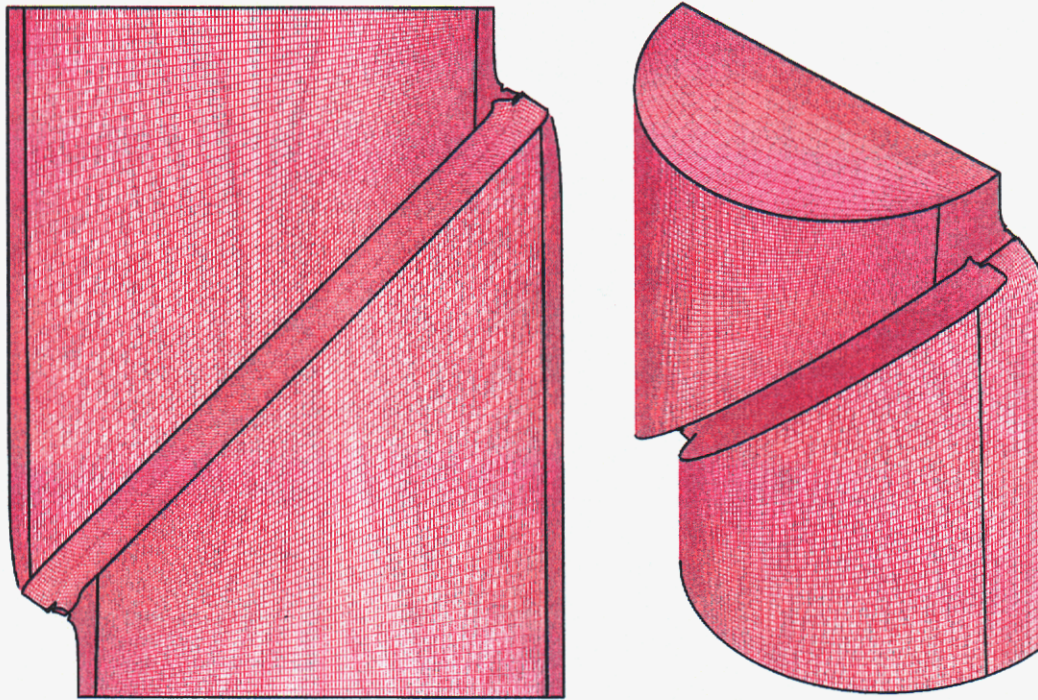


Figure 25. Simulation of 6061-T6 SCS Experiment (Pronto3D with BCJ; 334,132 elements): 1.6 mm slot width, 0.13 mm fillet radius, 0.13 mm EDM cutout radius

Figure 26 shows contour plots of vonMises stress, equivalent plastic strain, and temperature. The dimensions of the sample are shown in Figure 8. Half-symmetry is used. The top face velocity was specified at 25 m/s for a total of 100 microseconds. Existing BCJ constants were used (Taylor 1996).

For the Ti-6Al-4V torsional Kolsky specimen simulation, new BCJ constants were determined from experimental data by (Lindholm et al. 1968). The comparison between data and model is shown in Figure 27. Other material constants at 293K used for Ti-6Al-4V are shown in Table 3, from Touloukian & DeWitt (1970) and Brandes & Brook (1992).

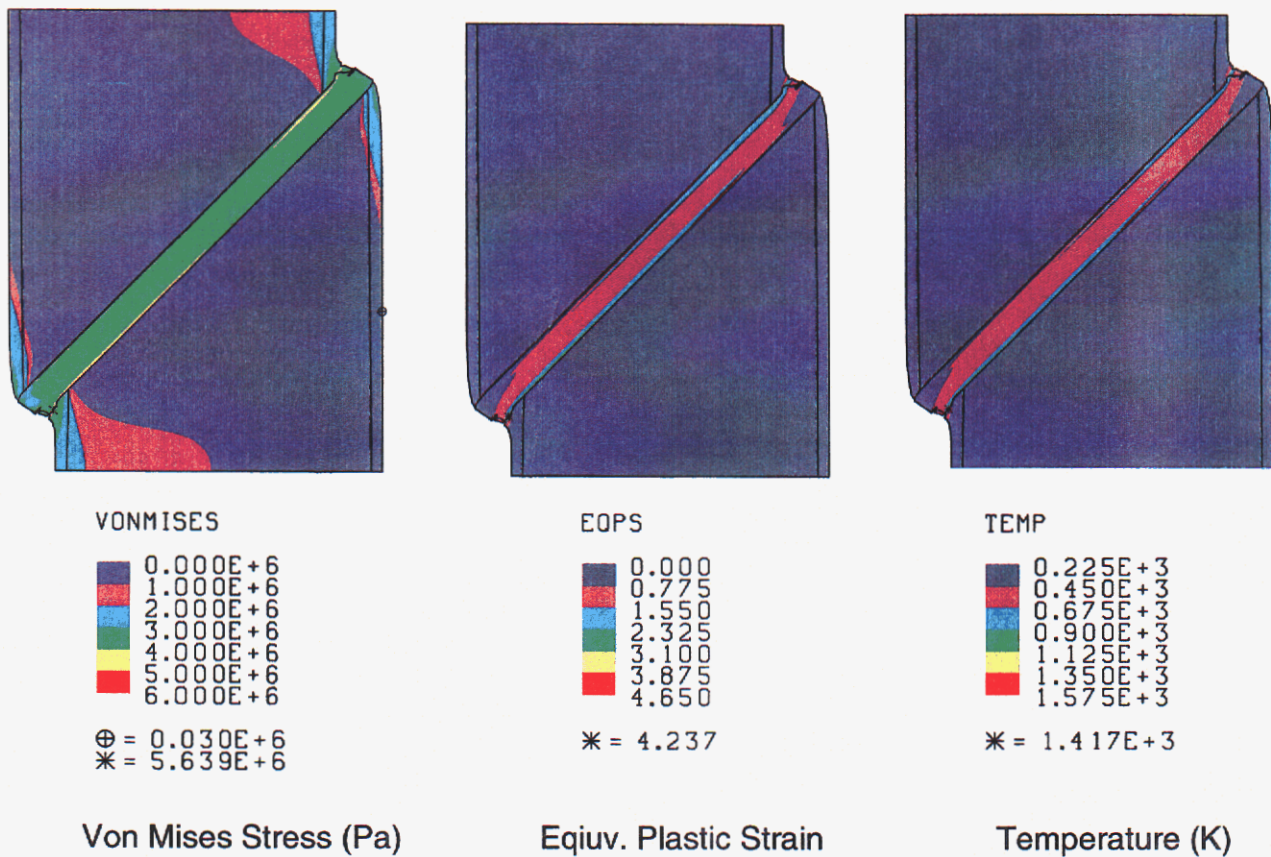


Figure 26: Contour plots for 6061-T6 SCS specimen simulation.

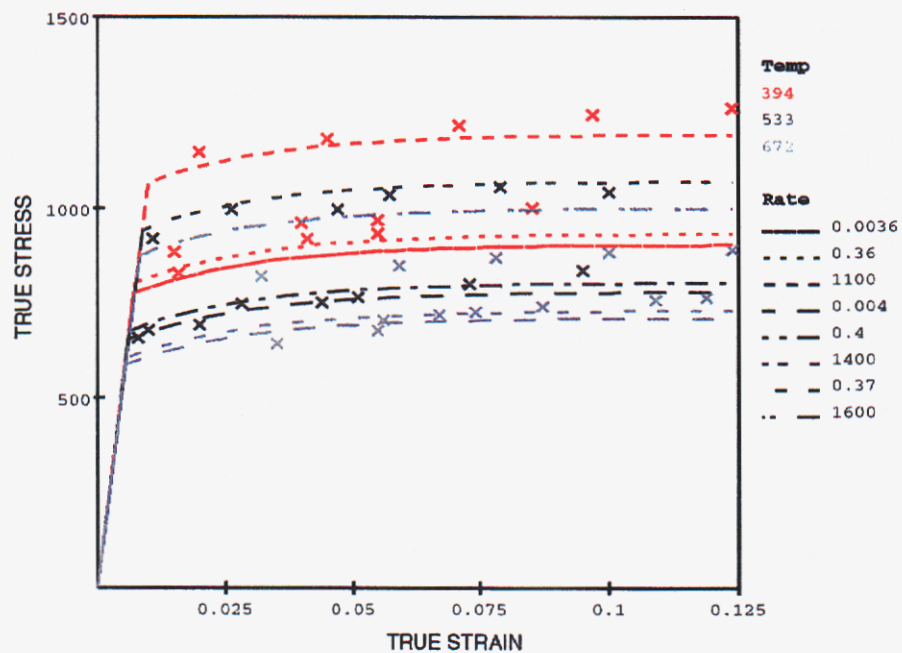


Figure 27: Comparison of experimental data for Ti-6Al-4V from Lindholm et al. 1968 (X's) to BCI model (lines). Stress in MPa.

Young's Modulus	106 GPa
Poissons Ratio	0.33
Mass density	4422 kg/m ³
Thermal expansion coefficient	8.7e-6 /K
Thermal conductivity	7.22 W/mK
Specific heat	531.0 J/kgK
Stefan Boltzman constant	5.68e-8 W/K ⁴ m ²
Emissivity	0.15

Table 3. Other material constants for Ti-6Al-4V

To reduce the computational effort, a slice mesh was approximated for the full three-dimensional thin wall tube as shown in Figures 28 and 29. The top face twist rate was specified at 180 rad/s, and a 1.0 m/s velocity was applied to the top face of the slice to approximate the twist rate. Cal Tech reported that a typical torsional Kolsky test lasted about 400 microseconds. Without any geometric defect introduced into the mesh, the results were compared between the two meshes. In Figs. 28 and 29, comparing von Mises stress, equivalent plastic strain, and temperature shows the slice mesh approximation is adequate. To investigate the effects of a meshed geometric defect and a coupled elastodynamic/heat conduction analysis, the slice mesh was used.

Pronto3D and Abaqus Explicit elastodynamic simulations using the BCJ model match exactly for the one element uniaxial compression case as shown in Fig. 30. The Abaqus Explicit User Material Subroutine interface, however, does not yet work for the coupled elastodynamic/heat conduction analysis using hourglass controlled hexahedral elements (Belytschko & Bindeman 1993). As a result, an inherent temperature dependent power-law hardening model was used instead of the BCJ model as for the previous simulations. Material constants for the power-law hardening model were estimated from the existing BCJ model constants, and, as a result, only a qualitative comparison of adiabatic elastodynamic analysis to coupled elastodynamic/heat conduction analysis using Abaqus Explicit could be conducted.

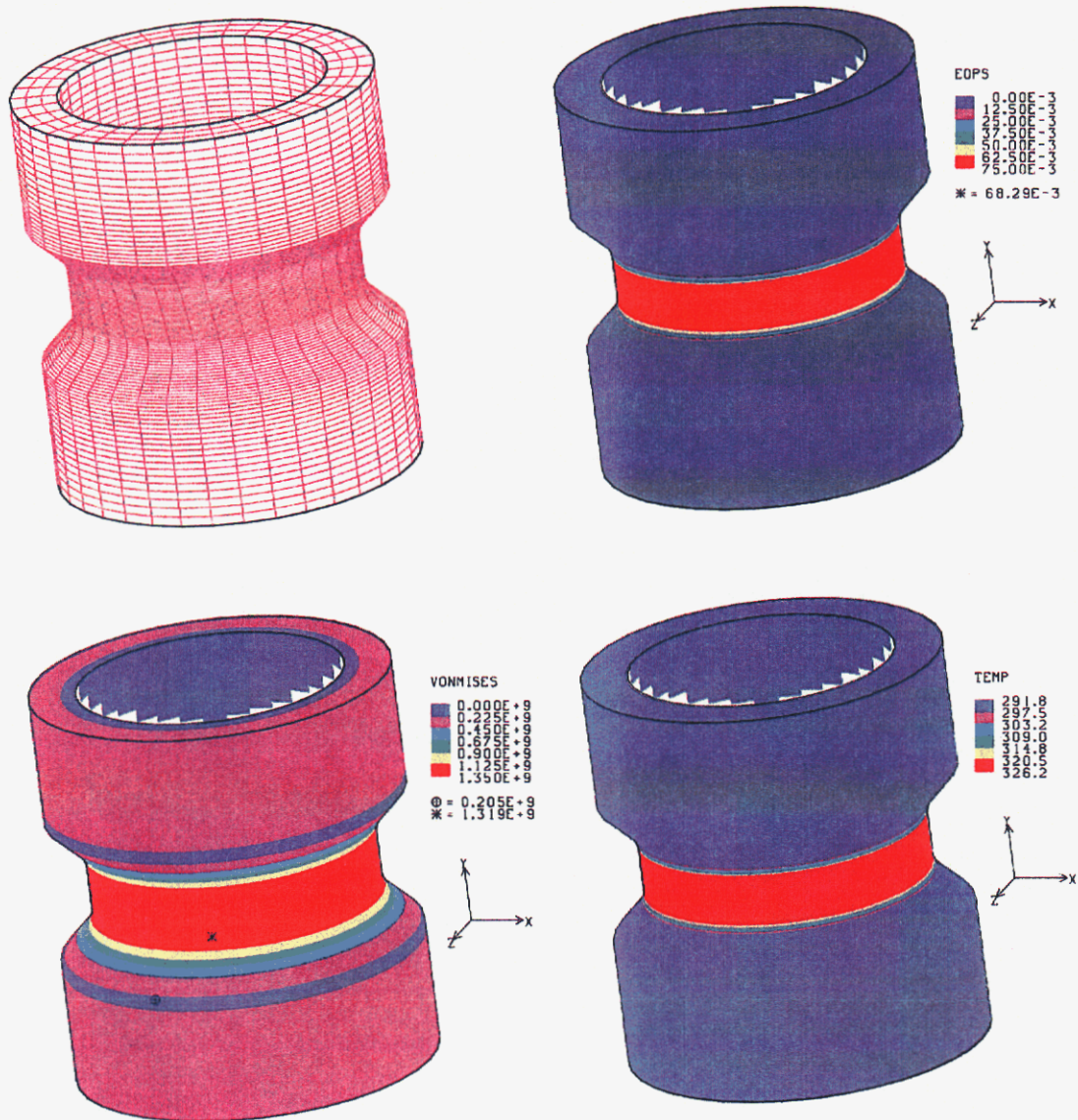


Figure 28: Full 3D simulation of Ti-6Al-4V torsional Kolsky specimen. Input torsional pulse of 180 rad/s for 400 μ s. Max. plastic strain is 6.8%, max. effective stress is 1.32 GPa, max. temperature is 326K.

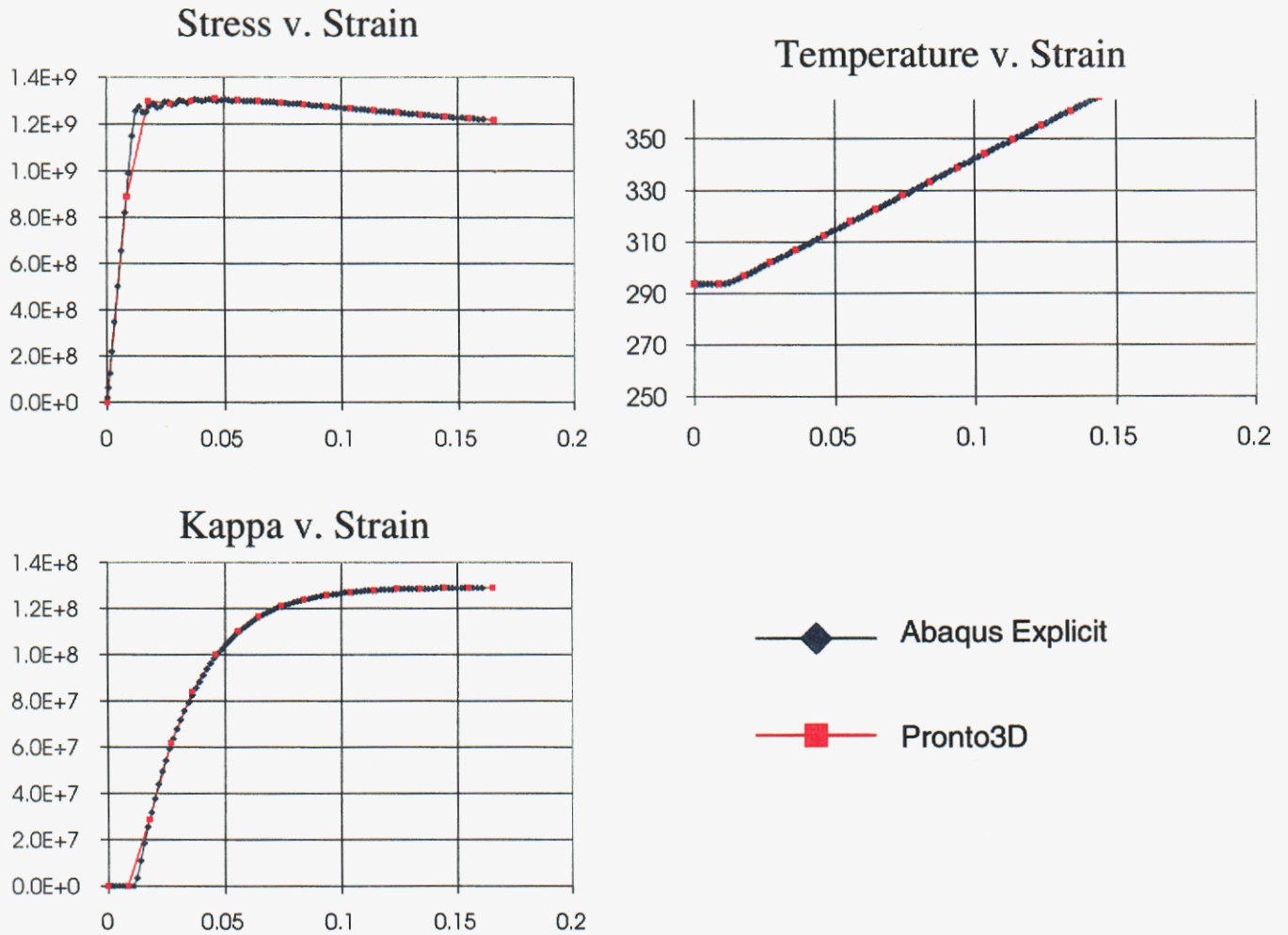


Figure 30: Comparison of Pronto3D and Abaqus Explicit One Element Uniaxial Compression Simulations (Ti-6Al-4V with BCJ). They compare almost exactly. Units are Pascals and Kelvin. Strain rate is 900/s.

Figure 31 shows the deformed meshes from Pronto3D with three mesh refinements and meshed defect: for 1,998, 10,944, and 33,696 hexahedral elements. Figure 32 shows the deformed 1,998 element mesh using Abaqus Explicit and a power-law hardening model. The meshed defect is a kink on the order of 2.5% the wall thickness (10 μm deep kink compared to 380 μm thick wall). Mesh-dependent behavior was observed, most likely because the mesh size was not refined to the inherent length scale of the rate-and-temperature-dependent constitutive model. Force versus displacement and shear stress versus shear strain plots in Figure 33 demonstrate mesh-dependence as the finer meshes localize earlier. There does not appear to be convergence to a critical localized displacement as the mesh is refined.

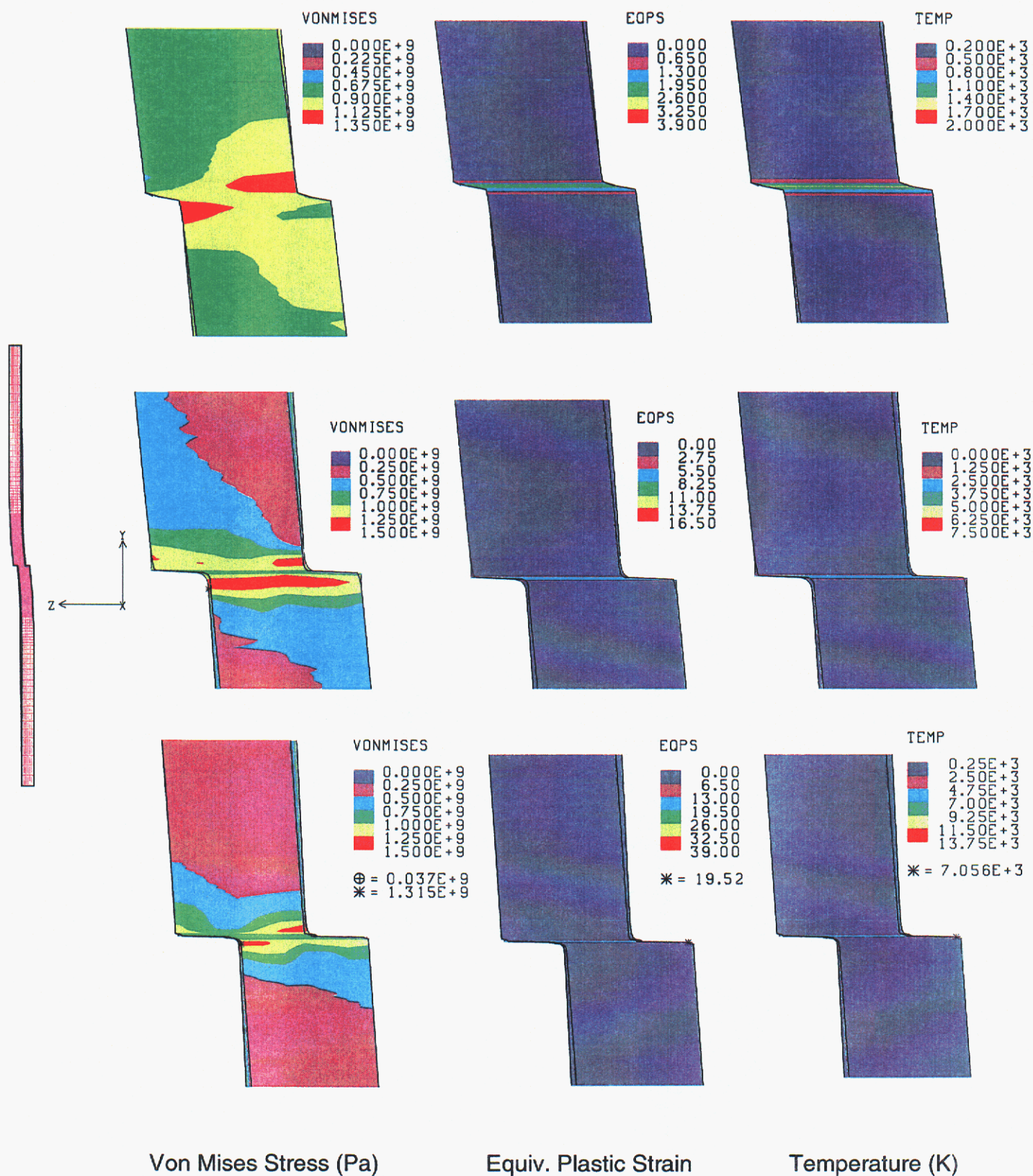


Figure 31: Pronto3D slice simulations for 1,998, 10,944, and 33,696 hexahedral elements with kink defect.

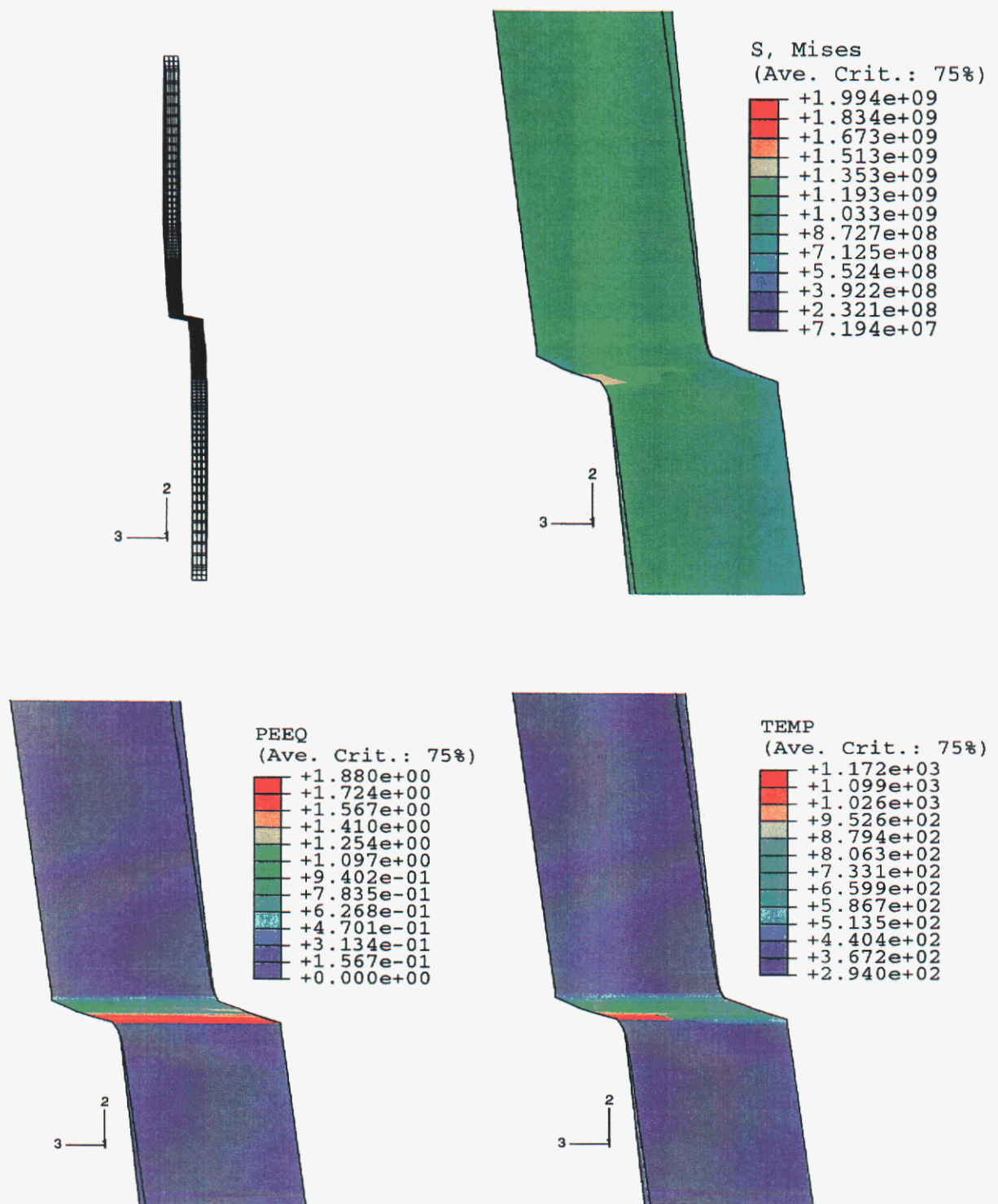


Figure 32: Abaqus Explicit slice simulation contour plots for 1,998 element elastodynamic analysis using power-law hardening model.

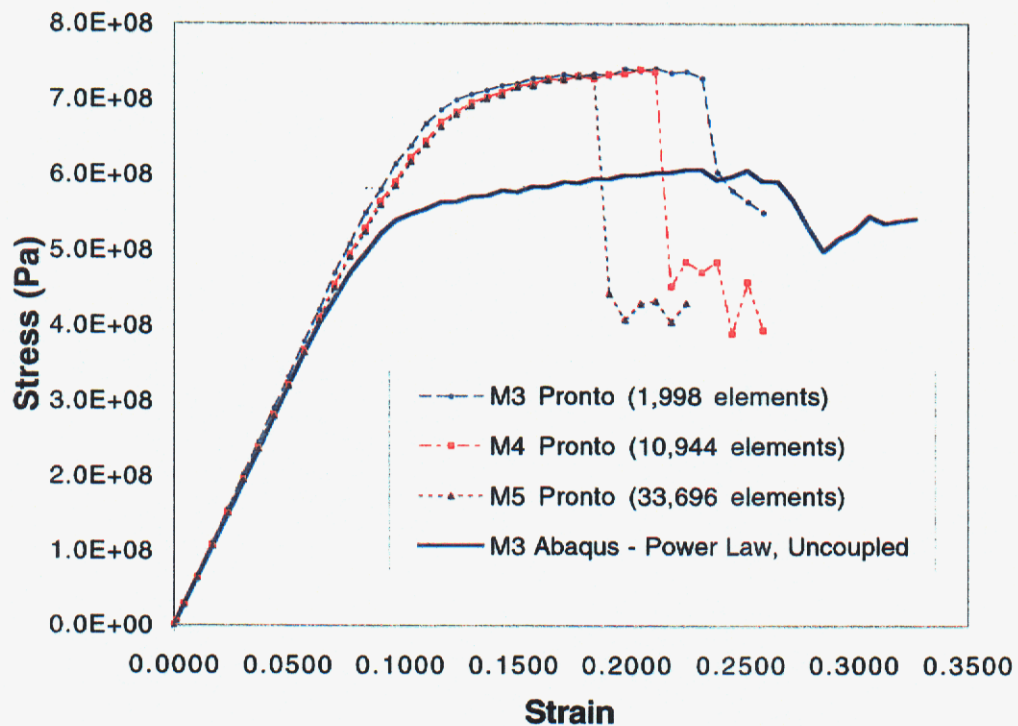
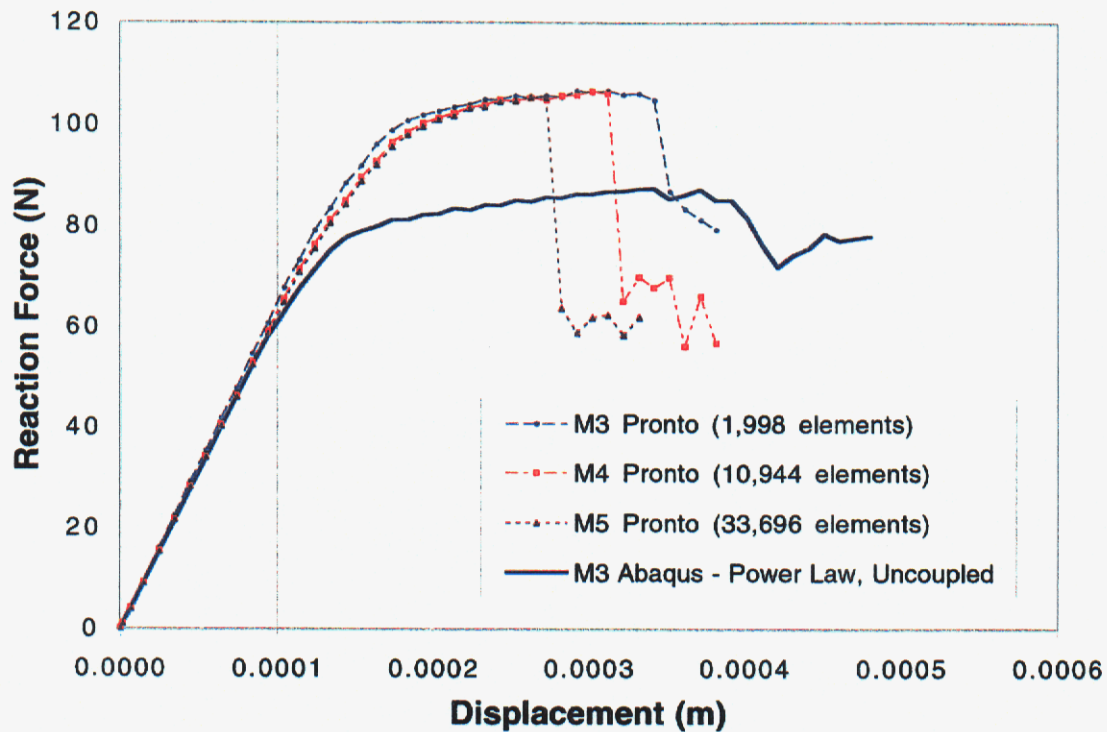


Figure 33: Force vs. Displacement (and Shear stress vs. Shear strain) plots for comparison of Pronto3D (with BCJ) and Abaqus Explicit (with power-law hardening) slice simulations with kink defect. Note the mesh-dependence as the mesh is refined.

Coupled Elastodynamic/Heat Conduction Analysis

A coupled elastodynamic/heat conduction analysis using Abaqus Explicit was run for the torsional Kolsky mesh and compared to the elastodynamic adiabatic analysis. There was little difference between the two simulations, although the uncoupled analysis demonstrated localized deformation slightly earlier with an apparently less stable post-localization response than the coupled analysis, which is consistent with the observed numerical stabilization of heat conduction. Abaqus Explicit was used because currently there is no coupled Pronto/Coyote code nor a coupled Presto/Calore code.

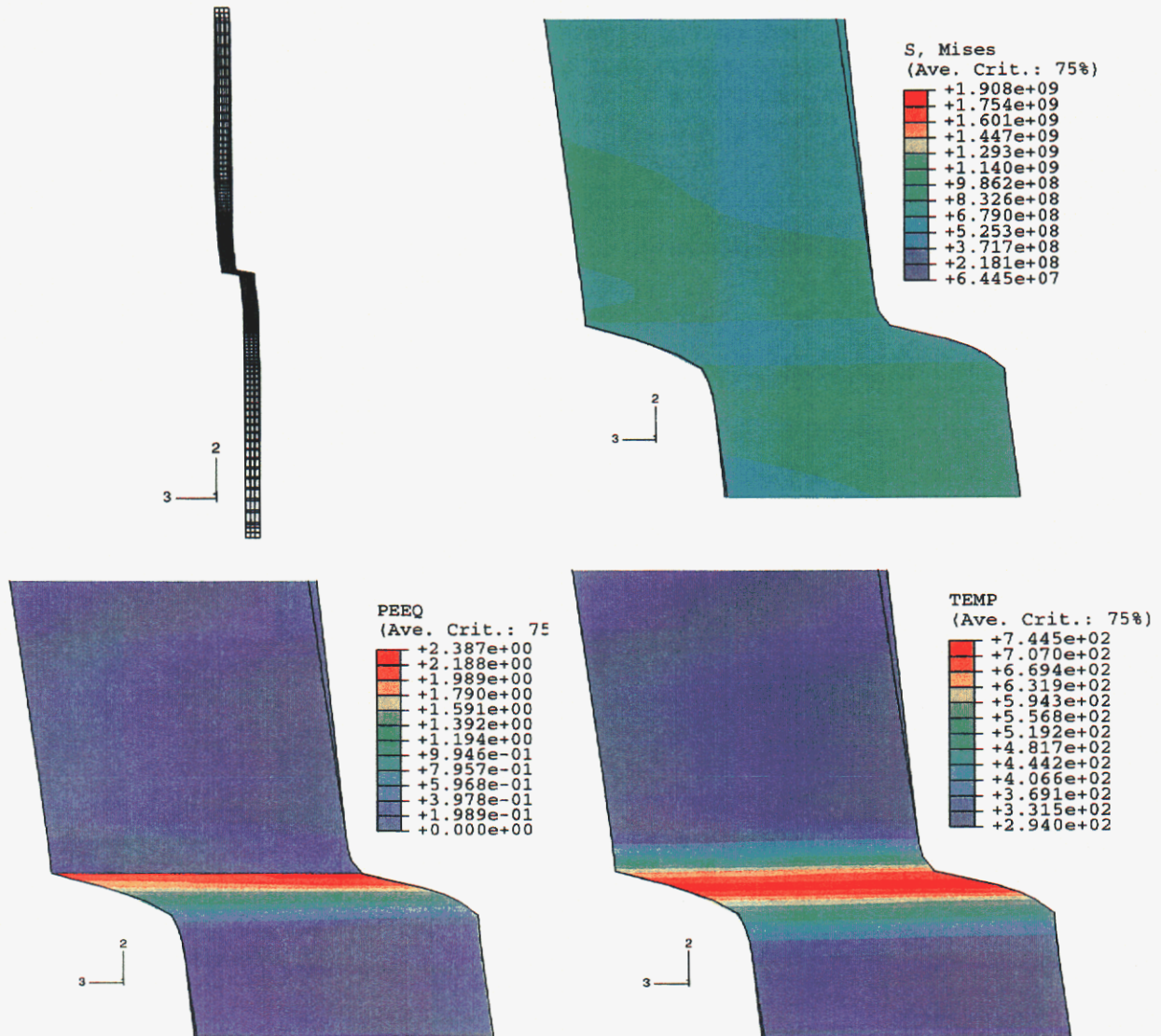


Figure 34: Abaqus Explicit slice simulation contour plots for 1,998 element coupled elastodynamic/heat conduction simulation with power-law hardening model.

Figures 34 and 35 show the results of the coupled elastodynamic/heat conduction analysis and the comparison of the coupled and uncoupled results. The adiabatic elastodynamic analysis (uncoupled) demonstrated localized deformation and softening slightly earlier than the coupled elastodynamic/heat conduction analysis, but the addition of heat conduction along with the high loading rate did not preclude shear banding. A mesh refinement study was not conducted for the coupled elastodynamic/heat conduction analyses to see whether the simulations are mesh-dependent. It is advised that such a refinement study be conducted with a coupled Presto/Calore capability in Sierra using the BCJ model.

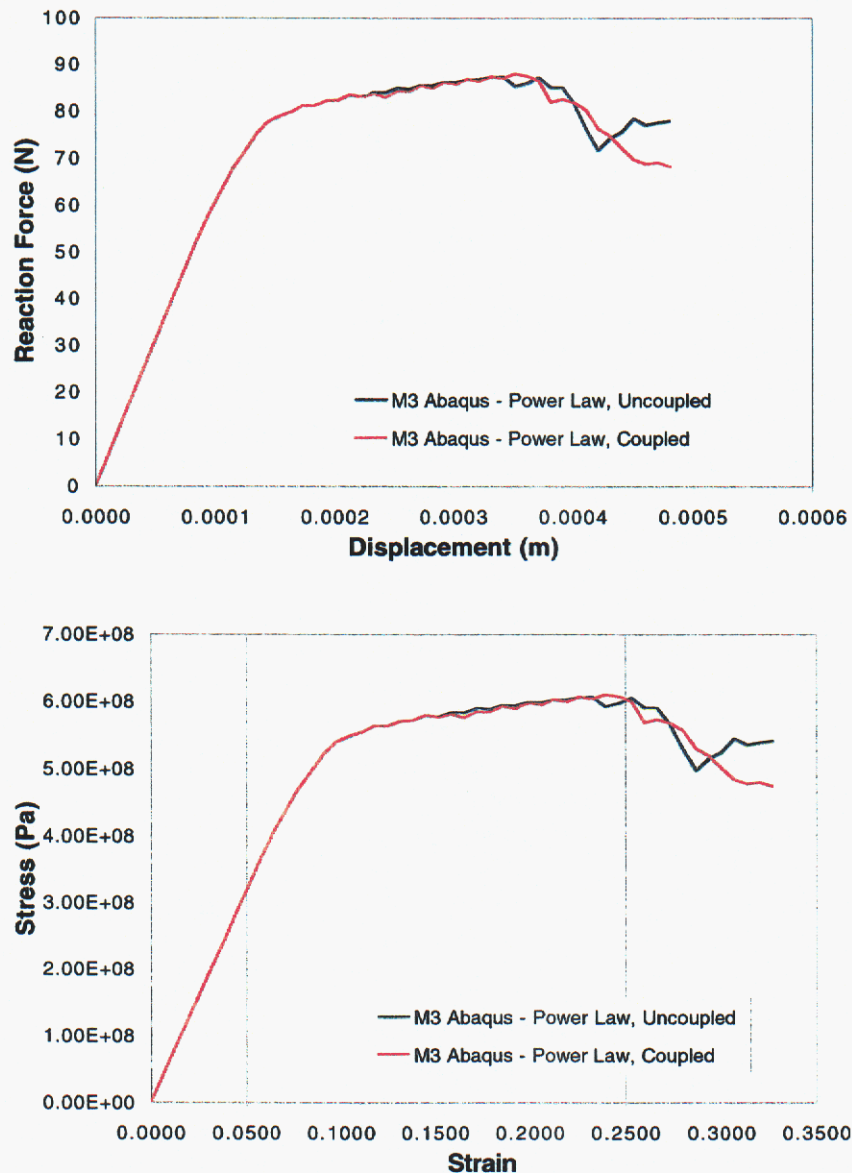


Figure 35: Force vs. Displacement (and Shear stress vs. Shear strain) plots for comparison of uncoupled and coupled Abaqus Explicit slice simulations.

Discussion

This project was not successful in developing a test method that could be used to generate quantitative data of the sort required to fully characterize susceptibility to adiabatic shear failure in alloys exhibiting a wide range of susceptibility. This was not entirely unexpected, given what was already known about the conflicting requirements of such a test. For techniques and specimen geometries capable of generating quantitative data of the required type, there are typically limitations to the range of conditions for which they can be used.

On the other hand, a promising new test geometry, the Shear Compression Specimen or SCS, has been identified and evaluated. While a capability for thoroughly characterizing adiabatic shear failure has not yet been shown for the SCS, it has demonstrated great promise for characterizing plastic deformation behavior over a wide range of strain rates. Comparison of experimental SCS and cylindrical compression data for 1018 steel (this project, Figure 13) and OFHC copper (Rittel et al. 2002b) indicates that a principal objective for the SCS specimen is achieved: accurate measurement of deformation property data over a wide range of strain rates with a single technique. To some degree, the same can also be said of cylindrical specimens tested quasi-statically and dynamically. However, note that significantly higher strain rates can be achieved with the SCS (47,000/s for 1018 steel vs. less than 10,000 for cylindrical compression SHPB tests), and that the SCS is better able to bridge the quasi-static-to-dynamic “gap” between rates of 10/s and 100/s.

A major factor in achieving a wide range of strain rates with the SCS specimen is the ability to combine loading rate and specimen slot width to reach a specific strain rate. Tests conducted for this project have shown that while results for different slot widths are similar at the same rate, there is a trend toward lower measured stress values for narrower slot widths. This issue should be investigated further. An additional issue for tests conducted to failure (including adiabatic shear tests) is the tendency for shear failures to run along the edge rather than the center of the gage section.

To obtain more complete data related to the initiation of adiabatic shear bands, SCS tests need to be conducted to a point at or just short of band initiation. While this can be accomplished in theory by modifying the input pulse, a more effective method is to use stop rings or a similar technique to provide a positive limit to specimen loading.

Designing an experimental specimen that demonstrates adiabatic shear failure in a variety of metals in a repeatable manner will most likely require machining geometric inhomogeneities in the specimen, such as grooves or indentations. Geometric inhomogeneities would initiate adiabatic shear failure in the experimental specimen in a repeatable manner with well-defined zones of uniform plastic deformation before localization, such that each experimental specimen of the same metal would experience similar location and orientation of shear banding. Introducing such geometric

inhomogeneities in the finite element mesh would generate shear banding with similar location and orientation as in the experiment. However, unless the finite element size is refined to the implicit length scale inherent in a thermo-elasto-viscoplasticity model (in this case, the local BCJ model), we would obtain mesh-dependent numerical solutions.

The same simulation issue is associated with implementing a physically-based nonlocal adiabatic shear band constitutive model: the finite element mesh would need to be refined (and possibly aligned with the shear band orientation) down to the physical length scale of the shear band in order to detect its initiation and track its propagation properly. This assumes that the constitutive model leads to a well-posed system of governing partial differential equations (elastodynamic or coupled elastodynamic/heat conduction). There are new numerical methods (Hughes et al. 1998; Garikipati & Hughes 2000; Liu et al. 1999) capable of capturing the “fine scale” effects of the physics (in this case the adiabatic shear band) at the “coarse scale” within the finite element or nodal influence region. These are powerful methods because the spatial discretization would not need to be refined to the physical length scale of the shear band (possibly on the order of 10 μm) in order to represent its effect in a convergent manner with respect to spatial discretization.

Additional constitutive modeling and numerical implementation issues that eventually should be addressed in order for a predictive physical model of adiabatic shear failure to be developed are 1) potential phase transformation of the material within the shear band, and 2) transition from shear band to fracture surface.

Conclusions and Recommendations

- Development of a single test method that is capable of evaluating adiabatic shear susceptibility over a wide range of susceptibilities remains an elusive goal. Principal problems include the difficulty in inducing failure in highly resistant alloys, and the influence of defects on the behavior of highly susceptible alloys.
- The Shear Compression Specimen, a promising new technique for evaluating deformation behavior over a wide range of strain rates, has been identified and evaluated.
- Recommendations for further study of the Shear Compression Specimen include use of stop rings for evaluation of adiabatic shear initiation.
- A rate-and-temperature-dependent constitutive model (BCJ model) with properly determined material constants could aid in understanding—but not predict—the onset of adiabatic shear banding, assuming that the finite element analysis is mesh-independent and has realistic geometric and/or material inhomogeneities to trigger shear banding.
- For modeling onset and post-localization behavior, we would need a shear band mode of deformation included in a nonlocal plasticity model to represent shear band

response and free surface creation (and possibly phase transformation) in a mesh-independent manner.

- Fully coupled elastodynamic/heat conduction finite element analyses should be considered for making engineering design decisions when a significant portion of inelastic deformation is converted to heat and thus has the ability to generate adiabatic shear banding and potential failure.

References

1. Affouard, J. L., Dormeal, R., Stelly, M., and Ansart, J. P., "Adiabatic shear bands in metals and alloys under dynamic compressive conditions," in *Mechanical Properties at High Rates of Strain, 1984*, held in Oxford, Harding, J., ed., pp. 533-537. The Institute of Physics, Bristol, 1984.
2. Backman, M. E. and Finnegan, S. A., "The propagation of adiabatic shear," in *Metallurgical Effects at High Strain Rates*, Rohde, R. W., Butcher, B. M., Holland, J. R., and Karnes, C. H., eds., pp. 531-541. Plenum Press, New York, 1973.
3. Backman, Marvin E. and Goldsmith, Werner "The mechanics of penetration of projectiles into targets," *International Journal of Engineering Science*, vol. 16, pp. 1-100, 1978.
4. Bai, Y. and Dodd, B., *Adiabatic Shear Localization: Occurrence, Theories, and Applications*. Pergamon Press, Oxford, 1992.
5. Bai, Y. L. and Johnson, W. "Plugging: Physical understanding and energy-absorption," *Metals Technology*, vol. 9, pp. 182-190, 1982.
6. Bammann, D. J. "Modeling the temperature and strain rate dependent large deformation of metals," *Applied Mechanics Reviews*, vol. 43, pp. S312-S319, 1990.
7. Bammann, D. J., Chiesa, M. L., and Johnson, G. C., "Modeling large deformation and failure in manufacturing processes," in *Proceedings of the XIXth International Congress on Theoretical and Applied Mechanics*, Tatsumi, T., ed., pp. 359-376. Elsevier, New York, 1996.
8. Batra, R. C., Adulla, C., and Wright, T. W. "Effect of Defect Shape and Size on the Initiation of Adiabatic Shear Bands," *Acta Mechanica*, vol. 116 (1-4), pp. 239-243, 1996.
9. Batra, R. C., Zhang, X., and Wright, T. W. "Critical Strain Ranking of 12 Materials in Deformations Involving Adiabatic Shear Bands," *Transactions of the*

ASME, vol. 62, pp. 252-255, 1995.

10. Bayoumi, A. E. and Xie, J. Q. "Some Metallurgical Aspects of Chip Formation in Cutting Ti-6Al-4V Alloy," *Materials Science & Engineering, A: Structural Materials: Properties, Microstructure and Processing*, vol. 190 (1-2), pp. 173-180, 1995.
11. Beatty, J. H., Meyer, L. W., Meyers, M. A., and Nemat-Nasser, S., "Formation of controlled adiabatic shear bands in AISI 4340 high strength steel," in *Shock Waves and High-Strain-Rate Phenomena in Metals*, Meyers, Marc A., Murr, Lawrence E., and Staudhammer, Karl P., eds., pp. 645-656. Marcel Dekker, New York, 1992.
12. Bedford, A. J., Wingrove, A. L., and Thompson, K. R. L. "The Phenomenon of Adiabatic Shear Deformation," *Journal of the Australian Institute of Metals*, vol. 19 (1), pp. 61-73, 1974.
13. Belytschko, T. and Bindeman, L. P. "Assumed strain stabilization of the eight node hexahedral element," *Computer Methods in Applied Mechanics and Engineering*, vol. 105, pp. 225-260, 1993.
14. Brandes, E. A. and Brook, G. B., eds., *Smithells Metal Reference Book*. Butterworth-Heinemann, Great Britain, 1992.
15. Campbell, J. D. and Ferguson, W. G. "The temperature and strain-rate dependence of the shear strength of mild steel," *Philosophical Magazine*, vol. 21, pp. 63-83, 1970.
16. Chen, L. and Batra, R. C. "Shear Instability Direction at a Crack Tip in a Thermoviscoplastic Body," *Theoretical and Applied Fracture Mechanics*, vol. 29 (1), pp. 33-40, 1998.
17. Clifton, R.J. and Klopp, R.W., "Pressure-shear plate impact testing," in *ASM Handbook, 8th Edition*, vol. 8: Mechanical Testing, pp. 230-238. ASM International, Metals Park, OH, 1985.
18. Corbett, G. G., Reid, S. R., and Johnson, W. "Impact loading of plates and shells by free-flying projectiles: A review," *International Journal of Impact Engineering*, vol. 18 (2), pp. 141-230, 1996.
19. Cowie, J. G., Azrin, M., and Olson, G. B. "Microvoid Formation during Shear Deformation of Ultrahigh Strength Steels," *Metallurgical Transactions A: Physical Metallurgy and Materials Science*, vol. 20A, pp. 143-153, 1989.
20. Culver, R. S. "Torsional-impact apparatus," *Experimental Mechanics*, vol. 12, pp. 398-405, 1972.
21. Curran, D. R., Seaman, L., and Shockey, D. A. "Dynamic Failure of Solids,"

Physics Reports, vol. 147, pp. 253-388, 1987.

22. Dikshit, S. N., Kutumbarao, V. V., and Sundararajan, G. "The Influence of Plate Hardness on the Ballistic Penetration of Thick Steel Plates," *International Journal of Impact Engineering*, vol. 16 (2), pp. 293-320, 1995.
23. Eleiche, A. M. and Duffy, J. "Effects of temperature on the static and dynamic stress-strain characteristics in torsion of 1100-O aluminum," *International Journal of Mechanical Sciences*, vol. 17, pp. 85-95, 1975.
24. Garikipati, K. and Hughes, T. J. R. "A variational multiscale approach to strain localization - formulation for multidimensional problems," *Computer Methods in Applied Mechanics and Engineering*, vol. 188, pp. 39-60, 2000.
25. Kuhn, Howard and Medlin, Dana, eds., *ASM Handbook*. ASM International, Metals Park, OH, 2000.
26. Giovanola, Jacques H. "Adiabatic shear banding under pure shear loading, Part I: Direct observation of strain localization and energy dissipation measurements," *Mechanics of Materials*, vol. 7, pp. 59-71, 1988a.
27. Giovanola, Jacques H. "Adiabatic shear banding under pure shear loading, Part II: Fractographic and metallographic observations," *Mechanics of Materials*, vol. 7, pp. 73-87, 1988b.
28. Grebe, H. A., Pak, H.-R., and Meyers, M. A. "Adiabatic Shear Localization in Titanium and Ti-6 Pct Al-4 Pct V Alloy," *Metallurgical Transactions A: Physical Metallurgy and Materials Science*, vol. 16A, pp. 761-775, 1985.
29. Hartley, K.A., Duffy, J., and Hawley, R.H., "The torsional Kolsky (Split-Hopkinson) bar," in *ASM Handbook: Volume 8, Mechanical Testing*, pp. 218-228. ASM International, Metals Park, OH, 1985.
30. Hartmann, K.-H., Kunze, H. D., and Meyer, L. W., "Metallurgical effects on impact loaded materials," in *Shock Waves and High-Strain-Rate Phenomena in Metals*, Meyers, M. A. and Murr, L. E., eds., pp. 325-337. Plenum Press, New York, 1981.
31. Hoke, D. A.: private communication, 1998.
32. Hughes, T. J. R., Feijoo, G. R., Mazzei, L., and Quincy, J.-B. "The variational multiscale method - a paradigm for computational mechanics," *Computer Methods in Applied Mechanics and Engineering*, vol. 166, pp. 3-24, 1998.
33. Kalthoff, J. F. and Winkler, S., "Failure mode transition at high strain rates of loading," in *Proceedings of the International Conference on Impact Loading and Dynamic Behavior of Materials*, Chiem, C. Y., Kunze, H. D., and Meyer, L. W., eds., pp. 185-195. Deutsche Gesellschaft für Metallkunde, DGM, Bremen, 1988.

34. Klepaczko, J. R. "Plastic Shearing at High and Very High-Strain Rates," *Journal de Physique IV*, vol. 4 (#C8), pp. 35-40, 1994.
35. Klepaczko, J. R. "Remarks on Impact Shearing," *Journal of the Mechanics and Physics of Solids*, vol. 46 (10), pp. 2139-2153, 1998.
36. Komanduri, R., Schroeder, T., Hazra, J., von Turkovich, B. F., and Flom, D. G. "On the Catastrophic Shear Instability in High Speed Machining of an AISI 4340 Steel," *Journal of Engineering for Industry*, vol. 104, pp. 121-131, 1982.
37. Komanduri, R. and Von Turkovich, B. F. "New Observations on the Mechanism of Chip Formation When Machining Titanium Alloys," *Wear*, vol. 69, pp. 179-188, 1981.
38. Lee, W. S. and Lin, C. F. "Plastic Deformation and Fracture Behavior of Ti-6Al-4V Alloy Loaded with High Strain-Rate under Various Temperatures," *Materials Science & Engineering, A: Structural Materials: Properties, Microstructure and Processing*, vol. 241 (1-2), pp. 48-59, 1998.
39. Leech, Patrick W. "Observations of adiabatic shear band formation in 7039 aluminum alloy," *Metallurgical Transactions A: Physical Metallurgy and Materials Science*, vol. 16A, pp. 1900-1903, 1985.
40. Lemaier, J. C. and Backofen, W. A. "Adiabatic Instability in the Orthogonal Cutting of Steel," *Metallurgical Transactions*, vol. 3, pp. 477-481, 1972.
41. Liao, S. C. and Duffy, J. "Adiabatic Shear Bands in a Ti-6Al-4V Titanium Alloy," *Journal of the Mechanics and Physics of Solids*, vol. 46 (11), pp. 2201-2231, 1998.
42. Lindholm, U. S., Nagy, A., Johnson, G. R., and Hoegfeldt, J. M. "Large strain, high strain rate testing of copper," *Journal of Engineering Materials and Technology*, vol. 102, pp. 376-381, 1980.
43. *An investigation of the behavior of materials under high rates of deformation*, Air Force Materials Laboratory, Dayton, OH, 1968.
44. Liu, W. K., Hao, S., Belytschko, T., Li, S. F., and Chang, C. T. "Multiple scale meshfree methods for damage, fracture and localization," *Computational Materials Science*, vol. 16, pp. 197-205, 1999.
45. Marchand, A. and Duffy, J. "An Experimental Study of the Formation Process of Adiabatic Shear Bands in a Structural Steel," *Journal of the Mechanics and Physics of Solids*, vol. 36 (3), pp. 251-283, 1988.
46. Mason, C. R., Worswick, M. J., and Gallagher, P. J. "Adiabatic Shear in Remco Iron and Quenched and Tempered 4340 Steel," *Journal de Physique IV*, vol. 7 (#C3), pp. 827-832, 1997.

47. Mason, J. J., Rosakis, A. J., and Ravichandran, G. "Full Field Measurements of the Dynamic Deformation Field Around a Growing Adiabatic Shear Band at the Tip of a Dynamically Loaded Crack or Notch," *Journal of the Mechanics and Physics of Solids*, vol. 42 (11), pp. 1679-1697, 1994a.
48. Mason, J. J., Rosakis, A. J., and Ravichandran, G. "On the Strain and Strain-Rate Dependence of the Fraction of Plastic Work Converted to Heat: An Experimental Study Using High-Speed Infrared Detectors and the Kolsky Bar," *Mechanics of Materials*, vol. 17 (2-3), pp. 135-145, 1994b.
49. Meunier, Y., Roux, R., and Moureaud, J., "Survey of adiabatic shear phenomena in armor steels with perforation," in *Shock Waves and High-Strain-Rate Phenomena in Metals*, Meyers, Marc A., Murr, Lawrence E., and Staudhammer, Karl P., eds., pp. 637-644. Marcel Dekker, New York, 1992.
50. Meyer, L.W. and Manwaring, S., "Critical Adiabatic Shear Strength of Low Alloyed Steel Under Compressive Loading," in *Metallurgical Applications of Shock-Wave and High-Strain-Rate Phenomena*, L.E. Murr, K.P. Staudhammer, and M.A. Meyers, eds., eds., pp. 657-674. Marcel Dekker, Inc., New York, 1986.
51. Nicholas, T. and Lawson, J. E. "On the Determination of the Mechanical Properties of Materials at High Shear-Strain Rates," *Journal of the Mechanics and Physics of Solids*, vol. 20, pp. 57-64, 1972.
52. Prasad, Y. V. R. K. and Sasidhara, S., eds., *Hot Working Guide: A Compendium of Processing Maps*. ASM International, Materials Park, OH, 1997.
53. Recht, R. F. "Catastrophic Thermoplastic Shear," *Journal of Applied Mechanics*, vol. 31, pp. 189-193, 1964.
54. Rittel, D., Lee, S., and Ravichandran, G. "A shear-compression specimen for large strain testing," *Experimental Mechanics*, vol. 42 (1), pp. 58-64, 2002a.
55. Rittel, D., Ravichandran, G., and Lee, S. "Large strain constitutive behavior of OFHC copper over a wide range of strain-rates using the shear compression specimen," *submitted to Experimental Mechanics*, 2002b.
56. Roessig, K. M. and Mason, J. J. "Adiabatic Shear Localization in the Impact of Edge-Notched Specimens," *Experimental Mechanics*, vol. 38 (3), pp. 196-203, 1998.
57. Roessig, K. M. and Mason, J. J. "Adiabatic shear localization in the dynamic punch test, part I: experimental investigation," *International Journal of Plasticity*, vol. 15, pp. 241-262, 1999.
58. Rogers, H. C. "Adiabatic Plastic Deformation," *Annual Review of Materials Science*, vol. 9, pp. 283-311, 1979.

59. Rogers, H. C., "Adiabatic Shearing - General Nature and Material Aspects," in *Material Behavior Under High Stress and Ultrahigh Loading Rates*, Mescall, John and Weiss, Volker, pp. 101-118. Plenum Press, New York, 1983.
60. Rogers, H. C. and Shastry, C. V., "Material factors in adiabatic shearing in steels," in *Shock Waves and High-Strain-Rate Phenomena in Metals*, Meyers, M. A. and Murr, L. E., eds., pp. 285-297. Plenum Press, New York, 1981.
61. Sargent, P. M. and Ashby, M. F. *The Presentation of High Strain-Rates on Deformation Mechanism Maps*, Final Technical Report, July 1980-July 1982 on Contract DAJA37-80-C-0333, USARDSG-UK, 1983.
62. Semiatin, S. L. and Lahoti, G. D. "The occurrence of shear bands in non-isothermal hot-forging of Ti-6Al-2Sn-4Zr-2Mo-0.1Si," *Metallurgical Transactions A: Physical Metallurgy and Materials Science*, vol. 14 (1), pp. 105-115, 1983.
63. Semiatin, S. L., Lahoti, G. D., and Oh, S. I., "The Occurrence of Shear Bands," in *Material Behavior Under High Stress and Ultrahigh Loading Rates*, Mescall, John and Weiss, Volker, pp. 119-159. Plenum Press, 1983.
64. Shawki, T. G. "An Energy Criterion for the Onset of Shear Localization in Thermal Viscoplastic Materials, Part I: Necessary and Sufficient Initiation Conditions," *Journal of Applied Mechanics*, vol. 61, pp. 530-537, 1994a.
65. Shawki, T. G. "An Energy Criterion for the Onset of Shear Localization in Thermal Viscoplastic Materials, Part II: Applications and Implications," *Journal of Applied Mechanics*, vol. 61, pp. 538-547, 1994b.
66. Staker, M. R. "The Relation Between Adiabatic Shear Instability Strain and Material Properties," *Acta Metallurgica*, vol. 29, pp. 683-689, 1981.
67. Stelly, M. and Dornmeier, R., "Adiabatic shearing," in *Metallurgical Applications of Shock-Wave and High-Strain-Rate Phenomena*, L.E. Murr, K.P. Staudhammer, and M.A. Meyers, eds., eds., pp. 607-632. Marcel Dekker, Inc., New York, 1986.
68. Taylor, G. I. and Quinney, H. "The Latent Energy Remaining in a Metal after Cold Working," *Proceedings of the Royal Society of London, Series A: Mathematical and Physical Sciences*, vol. A143, pp. 307-326, 1934.
69. *CTH Reference Manual: The Bammann-Chiesa-Johnson Viscoplastic/Damage Model*, SAND96-1626, Sandia National Laboratories, Livermore, CA, 1996.
70. Timothy, S. P. "The Structure of Adiabatic Shear Bands in Metals: A Critical Review," *Acta Metallurgica*, vol. 35 (2), pp. 301-306, 1987.
71. Touloukian, Y. S. and DeWitt, D. P., eds., *Thermophysical Properties of Matter*. IFI/Plenum, New York, 1970.

72. Wingrove, A. L. "The influence of projectile geometry on adiabatic shear and target failure," *Metallurgical Transactions*, vol. 4, pp. 1829-1833, 1973.
73. Winter, R. E. "Adiabatic Shear of Titanium and Polymethylmethacrylate," *Philosophical Magazine*, vol. 31 (4), pp. 765-773, 1975.
74. Wittman, C. L., Meyers, M. A., and Pak, H.-r. "Observation of an Adiabatic Shear Band in AISI 4340 Steel by High-Voltage Transmission Electron Microscopy," *Metallurgical Transactions A: Physical Metallurgy and Materials Science*, vol. 21A, pp. 707-716, 1990.
75. Woodward, R. L. "Interrelation of failure modes observed in the penetration of metallic targets," *International Journal of Impact Engineering*, vol. 2 (2), pp. 121-129, 1984.
76. Woodward, R. L., Baxter, B. J., and Scarlett, N. V. Y., "Mechanisms of adiabatic shear plugging failure in high strength aluminium and titanium alloys," in *Mechanical Properties at High Rates of Strain, 1984*, held in Oxford, Harding, J., ed., pp. 525-532. The Institute of Physics, Bristol, 1984.
77. Wright, T. W. "Toward a Defect Invariant Basis for Susceptibility to Adiabatic Shear Bands," *Mechanics of Materials*, vol. 17 (2-3), pp. 215-222, 1994.
78. Wright, T. W. and Batra, R. C. "Further results on the initiation and growth of adiabatic shear bands at high strain rates," *International Journal of Plasticity*, vol. 1, pp. 205-212, 1985.
79. Wulf, G. L. "High-strain rate compression of titanium and some titanium alloys," *International Journal of Mechanical Sciences*, vol. 21 (12), pp. 713-718, 1979.
80. Zener, C. and Hollomon, J. H. *Journal of Applied Physics*, vol. 61, pp. 1816-1825, 1944.
81. Zhou, M., Ravichandran, G., and Rosakis, A. J. "Dynamically Propagating Shear Bands in Impact-Loaded Prenotched Plates - II. Numerical Simulations," *Journal of the Mechanics and Physics of Solids*, vol. 44 (6), pp. 1007-1032, 1996.
82. Zurek, A. K. "The Study of Adiabatic Shear-Band Instability in a Pearlitic 4340 Steel Using a Dynamic Punch Test," *Metallurgical Transactions A: Physical Metallurgy and Materials Science*, vol. 25A (11), pp. 2483-2489, 1994.

DISTRIBUTION:

3		California Institute of Technology Graduate Aeronautical Laboratories Attn: Prof. G. Ravichandran MS 105-50 1200 East California Blvd. Pasadena, CA 91125
1	MS 0188	C. E. Meyers, 1030
1	MS 9001	M. E. John, 8000 Attn: J. Vitko, 8100, MS 9004 D. R. Henson, 8200, MS 9007 W. J. McLean, 8300, MS 9054 P. N. Smith, 8500, MS 9002 K. E. Washington, 8900, MS 9003
10	MS 9042	D. B. Dawson, 8725
1	MS 9042	J. J. Dike, 8727
1	MS 9042	Y. Ohashi, 8727
1	MS 9042	A. R. Ortega (A), 8727
1	MS 9161	E-P Chen, 8726
1	MS 9401	J. M. Hruby, 8702
1	MS 9402	K. L. Wilson, 8703
1	MS 9404	J. R. Garcia, 8725
1	MS 9405	R. H. Stulen, 8700 Attn: B. Hwang, 8721, MS 9161 W. R. Even, 8722, 9403 J. C. F. Wang, 8723, MS 9403 C. H. Cadden, 8724, 9402 M. F. Horstemeyer, 8728, 9042 C. C. Henderson, 8729, MS 9401 J. E. M. Goldsmith, 8730, MS 9409 W. C. Replogle, 8731, MS 9409 G. D. Kubiak, 8732, MS 9409
1	MS 9405	R. A. Regueiro, 8726
3	MS 9018	Central Technical Files, 8945-1
1	MS 0899	Technical Library, 9616
1	MS 9021	Classification Office, 8511/Technical Library, MS 0899, 9616
1	MS 0188	D. Chavez, LDRD Office, 1030

